The Report Committee for Williams Osagie Ozowe
Certifies that this is the approved version of the following report:

Capillary Pressure Curve and Liquid Permeability Estimation in Tight Oil Reservoirs using Pressure Decline versus Time Data

APPROVED BY
SUPERVISING COMMITTEE:

Supervisor:

Mukul M. Sharma

Ryosuke Okuno

Capillary Pressure Curve and Liquid Permeability Estimation in Tight Oil Reservoirs using Pressure Decline versus Time Data

by

Williams Osagie Ozowe

Report

Presented to the Faculty of the Graduate School of

The University of Texas at Austin

in Partial Fulfillment

of the Requirements

for the Degree of

Master of Science in Engineering

The University of Texas at Austin

December, 2018

Dedication

This report is dedicated to my parents Fred and Patricia and to my siblings Justina, Victor, Kinglsey and Stella, for their unconditional love and support throughout my entire life. I would also like to dedicate this work to my loving wife Gladys who stood by me through the good, bad and ugly times, throughout the entire course of my graduate study, and to our lovely son Jason, you lighten up our world.

Acknowledgements

I would like to express my profound gratitude to my supervisor Dr. Mukul Sharma for his continuous encouragement, his kindness and his patience through this study. I learnt a lot from his vast wealth of experience in and out of this field of study. I would also like to thank Dr. Daigle for providing me the opportunity to work in his research lab and also to use some of his equipment during the course of the experiments in this research.

Special thanks to Mr. Rod Russell and Ms. Jin Lee for their overwhelming technical and administrative support throughout this experimental study. My appreciation also goes to Dr. David Medellin, who accepted to serve as my second reader and Dr. Chamy Miller for your valuable contribution and feedback on this work. Also, I would like to acknowledge the staff of the Petroleum and Geosystems Engineering Department at The University of Texas at Austin: Amy Douglas Stewart, John Cassibry, Jessica Yeager, Glen Baum, Gary Miscoe and Daryl Nygaard for their continued technical and administrative support.

In addition, I will like to extend my appreciation to all members of Dr. Sharma's graduate research group and my close friends for their love, understanding, support and encouragement. In particular, I would like to thank Weiwei Wu, Murtadha Al Tammar, Deepen Gala, Shawn Wu, Shuang Zeng and Connor Mulkay for all your support and company. I am also indebted to my friends, Saurab Tandon, Chris Griffith, Mayowa Oyedere, and others I do not cite explicitly for their moral and technical support.

Finally, special thanks go to my wife Chinwendu Gladys (Abaziem) Ozowe. I could never have achieved this without you. Thank you for your patience, sacrifice, understanding, kindness and above all your undying and endless love for me.

Abstract

Capillary Pressure Curve and Liquid Permeability Estimation in Tight Oil Reservoirs using Pressure Decline versus Time Data

Williams Osagie Ozowe, M.S.E.

The University of Texas at Austin, 2018

Supervisor: Mukul M. Sharma

Estimating oil recovery from shale is a difficult process because organic mudrocks have very low permeability (10nD – 100nD), high kerogen and clay content, a complex pore structure and low porosity (typically less than 10%). In addition, most of the pore sizes in organic mudrocks are within the nanometer range, thus making the process of oil intrusion very difficult to achieve and even harder to measure with certainty. Several methods have been proposed to estimate saturation profiles and capillary pressure curves in conventional rocks, but these methods fail in tight rocks because of the complexities inherent in these types of reservoirs.

This report presents a new method that makes use of the pressure decline versus time data to estimate the capillary pressure drainage curve in tight rocks. The method was used to estimate the capillary drainage curve for an Eagle Ford shale and it was also used to determine the shale's liquid permeability using the early time data of the pressure decline curve. The data obtained during the experiment could be used to estimate fluid saturations as a function of time which can be very useful in determining relative

permeability curves in the shale. This new procedure is easy, fast and can be reversed to estimate imbibition curves as well. It can be applied to both conventional and unconventional rocks and it can be useful in EOR experiments to estimate oil recovery as a function of time.

Furthermore, this report presents the use of NMR as a useful tool in examining fluid distributions and characterizing fluid types within tight rocks, via a combination of NMR T_1 and T_2 data.

Table of Contents

List of Tables xi

List of Figures xii

List of Illustrations xv

Chapter 1: Introduction 1

1.1 Background and Motivation 1

1.2 Research Objectives 3

1.3 Overview of Chapters 4

Chapter 2: Literature Review 6

2.1 Petrophysical concepts on capillary pressure 6

2.2 Uses of Capillary Pressure Curves 9

2.3 Static methods for measuring capillary pressure 9

2.4 Agreement between Static and Dynamic methods 11

2.6 Effect of Capillary Pressure on Fluid Density and Phase Behavior in Shale 12

2.9 Permeability Determination 14

2.9.4 Steady State Method 15

2.9.5 Transient Methods 15

2.9.5.1 Pulse decay method for core plugs 15

2.9.5.2 Pressure build-up method 16

2.9.5.3 Permeability on crushed samples 17

Chapter 3: Experimental Apparatus and Procedures 18

3.1 Experimental Procedure for the Oil Saturation Experiments 18

3.2 Crushed Shale Preparation 18

3.3 Fluid Preparation 18

3.4 Core Holder Preparation 19

3.5 Spontaneous Imbibition procedure 19

3.6 Capillary Pressure and Permeability experimental procedure 20

3.7 Procedure for the NMR experiments 20
3.8 description of experimental apparatus 21
3.8.1 Pumps.....21
3.8.1.1 Hydraulic pump 21
3.8.1.2 Vacuum Pump.....21
3.8.1.3 Continuous flow pump.....22
3.8.2 Valves 22
3.8.3 Tubing.....22
3.8.4 Pressure Indicator and Transducer.....22
3.8.4.1 Gauge Pressure Indicator 22
3.8.4.2 Differential Pressure Transducer 23
3.8.5 Accumulators 23
3.8.6 Weighing Balance.....24
3.8.7 Computer Software 24
3.8.8 Core Holder.....24
3.8.9 NMR Spectrometer 25
3.8.10 Air dehumidifying Unit.....25

Chapter 4: Permeability and Capillary Pressure Estimates in Tight Rocks.....26
4.1 Theoretical basis for the crushed shale permeability solution. 26
4.2 Result from the Permeability Experiment.....28
4.3 Theoretical basis for the capillary pressure curve estimation. 30
4.4 Result for the Capillary Pressure Experiment.....30

Chapter 5: Fluid Distribution using NMR Spectroscopy.....36
5.1 Longitudinal Relaxation.....36
5.1.1 Inversion Recovery 38
5.2 Transverse Relaxation.....39
5.2.1 Diffusion enhanced T2 relaxation.....43
5.3 Surface Relaxation 44
5.4 Application of NMR Data to EOR in Tight Oil Reservoirs.....45
5.5 T_2 Distributions and Pore Size Distribution.....47

5.6 Results from Oil Intrusion Experiments 48
5.7 Description of parameters used for the nmr spectrometry 53
5.7.1 Tau 53
5.7.2 T_2 max 53
5.7.3 Number of Echoes (NE) 53
5.7.4 Number of Points per Echoes 54
5.7.5 Relaxation Delay (RD) 54
5.7.6 Number of Scans 54
5.7.7 Receiver Gain 54
Chapter 6: Summary and Conclusion 56
6.1 Conclusions 56
6.2 Future Work 57
References 59

List of Tables

Table 4.1 Experimental parameters. 29

Table 4.2 Results from the capillary pressure curve experiment. 35

Table 5.1 Parameters used for both dodecane and water HI measurements 46

Table 5.2 Summary of results for Water. 46

Table 5.3 Summary of results for n-Dodecane. 47

Table 5.4 Parameters used for the NMR T_2 & T_1-T_2 experiment. 55

List of Figures

Figure 1.1 Oil demand – Historic and Projected, in quadrillion Btu (OPEC 2018).2

Figure 1.2 Global energy consumption by fuels – Historic and Projected, in quadrillion Btu (OPEC 2018). 2

Figure 1.3 Total U.S. annual crude oil production and oil production from major shale plays (EIA, 2017). 3

Figure 2.1 Illustration of three interfacial tensions 7

Figure 2.2 Illustration of liquid and gas as wetting phases. 8

Figure 2.3 Capillary pressure curves by static and dynamic methods in sandstone cores. (Brown 1951).....11

Figure 2.3 Capillary pressure curves by static and dynamic methods in limestone cores. (Brown 1951).....12

Figure 2.4 Phase envelopes showing the effect of Capillary Pressure for binary mixtures of methane and hexane. (Nojabaei et al, 2012). 13

Figure 2.5 Phase envelopes showing the effect of Capillary Pressure for binary mixtures of methane and other alkanes. (Nojabaei et al, 2012). 14

Figure 2.6 Effect of capillary pressure on the bubble point of Bakken oil (Nojabaei et al, 2012). 14

Figure 2.7 Schematic diagram of a typical pulse decay apparatus. (Cui et al. 2009) 16

Figure 2.8 Schematic diagram of a pycnometer apparatus. (Cui et al. 2009) 17

Figure 4.1 Pressure time decay data at 2000 psig 29

Figure 4.2 Pressure time decay data at 100 psig and lnPs-Poβ + 1 + P0-Pi6ββ + 1P0-Pi vs time 29

Figure 4.3 Pressure time decay data at 100 psi initial pressure 31

Figure 4.4 Pressure time decay data at 200 psi initial pressure 32
Figure 4.5 Pressure time decay data at 500 psi initial pressure 32
Figure 4.6 Pressure time decay data at 1000 psi initial pressure 33
Figure 4.7 Pressure time decay data at 3000 psi initial pressure 33
Figure 4.8 Pressure time decay data at 4000 psi initial pressure 34
Figure 4.9 Drainage capillary pressure curve. 34
Figure 4.10 Oil volume increments. 35
Figure 5.1 Longitudinal relaxation growth and decay curves. (Dunn et al. 2002) 37
Figure 5.2 Inversion and tilting using 180^0 and 90^0 pulses. (Dunn et al. 2002) 38
Figure 5.3 Schematic of an inversion recovery process. (Dunn et al. 2002) 39
Figure 5.4 Schematic of a Free Induction Decay (FID) pulse. (Dunn et al. 2002) 40
Figure 5.5 Illustration of the CPMG pulse sequence for T_2 measurement. (Chung, 1993) 42
Figure 5.6 Graphical representation of the CPMG spin echo train for T_2 measurements. (Dunn et al. 2002) 44
Figure 5.7 HI index measurements for water.....46
Figure 5.8 HI index measurements for n-Dodecane 47
Figure 5.9 T_2 distribution and cumulative T_2 distribution of dry shale 50
Figure 5.10 T_2 distribution and cumulative T_2 distribution of shale sample at 500psi 50
Figure 5.11 T_2 distribution and cumulative T_2 distribution of shale sample at 2000psi 51
Figure 5.12 T_2 distribution and cumulative T_2 distribution of shale sample at 4000psi 51
Figure 5.13 T_2 distribution of raw NMR signal before subtraction. 52

Figure 5.14 Differential T_2 distribution. 53

List of Illustrations

Illustration 3.1 Process flow schematic for the permeability and capillary pressure experiments. 23

Illustration 3.2 Laboratory setup for the permeability and capillary pressure experiments. 25

Chapter 1: Introduction

1.1 Background and Motivation

The International energy Outlook 2018 presented by the US Energy Information Administration (EIA) forecasts a growth in the total global energy consumption from 575 quadrillion British thermal units (Btu) in 2015 to 739 quadrillion Btu in 2040. This corresponds to a 29% growth in global energy consumption in 25 years. Oil and gas consumption is expected to increase by 22% from 320 quadrillion Btu in 2015 to 390 quadrillion Btu in 2040. Similarly, the reference case as projected by the Organization of Petroleum Exporting Countries (OPEC) in the World Oil Outlook in 2018 indicates a 33% growth in energy demand by 2040. Amidst the advocacy for alternative fuel sources, OPEC projects that oil and gas will still make up more than 50% of the global energy supply by 2040. Fossil fuels have been the dominant source of global energy since the late 19th century and amongst fossil fuel sources, oil and gas dominates because of its advantages over coal and because it still proves to be the only reliable source of energy. Thus, conventional reservoirs have been exploited to meet the ever-growing global energy demand. This exploitation has led to huge technological advancements in oil and gas exploration, as well as drilling and production.

Conventional reservoirs are reservoirs that can be exploited via traditional and less expensive drilling and production methods whereas unconventional reservoirs refer to reservoirs whose permeabilities are very low or the resource is more difficult to exploit. They include gas and oil shales, tight gas sands, heavy oil, coal bed methane, tar sands and gas hydrates etc. These reservoirs, require technologically advanced and specialized drilling and production methods, such as horizontal drilling and hydraulic fracturing in order to be economically viable. In 2017, the EIA in one of its forecasts,

projected that production from tight oil reservoirs would grow by about a million barrels per day until 2022 before a steady decline till 2050. In a more optimistic forecast, a total growth of about 9 million barrels per day was projected from now till 2050, with a sharp increase till 2025 and a slower growth till 2050. Both forecast however point to an increase in production from unconventional reservoirs in the coming years.

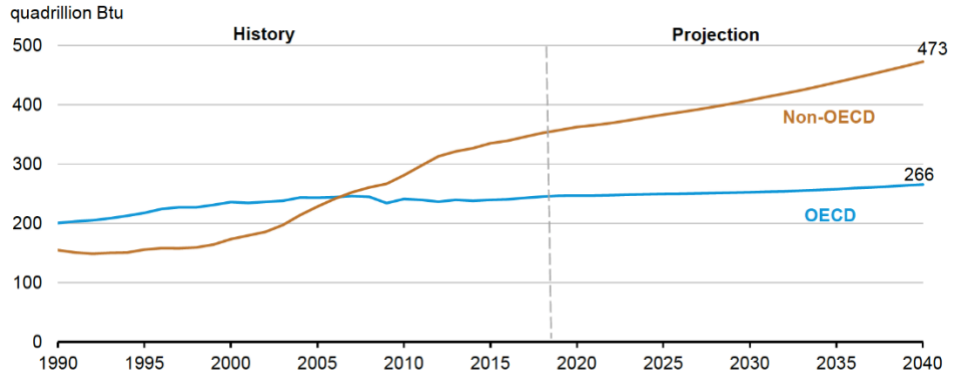

Figure 1.1 Oil demand – Historical and projected, in quadrillion Btu (OPEC 2018).

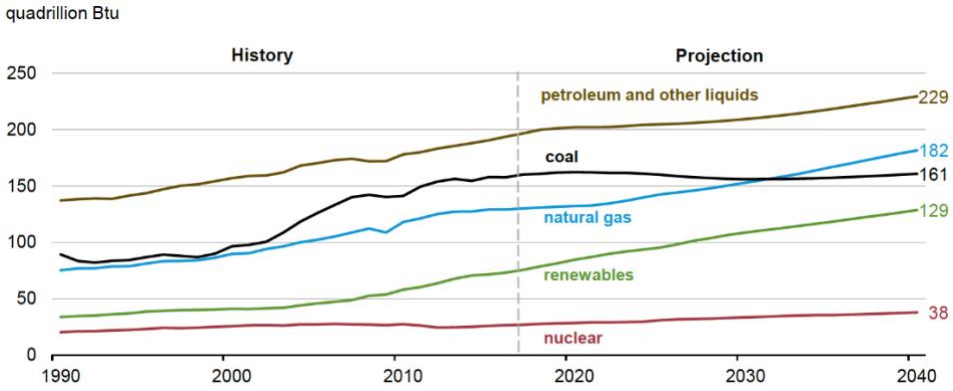

Figure 1.2 Global energy consumption by fuels – Historical and projected, in quadrillion Btu (OPEC 2018).

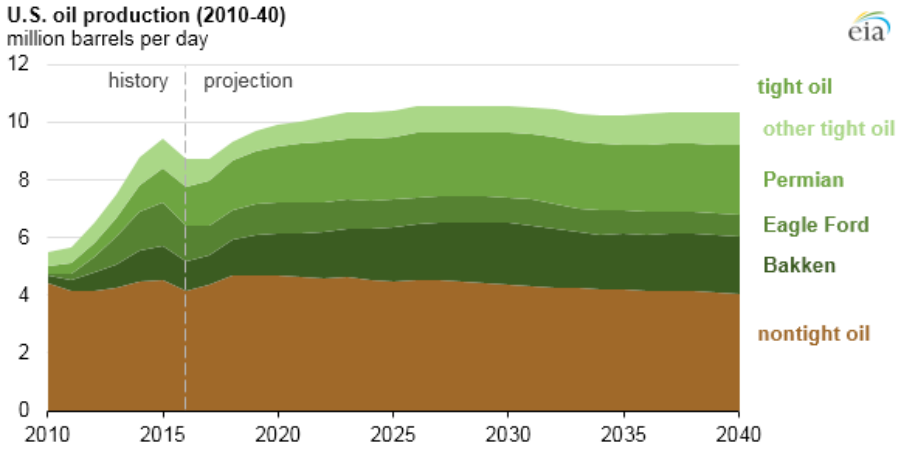

Figure 1.3 Total U.S. annual crude oil production and oil production from major shale plays (EIA, 2017).

Estimating oil recovery from unconventional reservoirs is a much more challenging process than in conventional reservoirs. Shale reservoirs in particular, prove more difficult because they have low porosity (about less than 10%), low permeability (10-100nD) high kerogen and clay content as well as a complex pore structure and pore network. In addition, most of the pore sizes in organic mudrocks are within the nanometer range, thus making the process of oil intrusion very difficult to achieve and even harder to measure with certainty. The need to have a close to accurate capillary pressure curve and permeability estimate cannot be over emphasized in unconventional reservoir simulations, because slight discrepancies in oil saturation could result in huge inconsistencies in predicted oil production.

1.2 Research Objectives

This research has three main objectives. The first is to develop a novel way of determining the capillary pressure curve for shale oil reservoirs using a dynamic method that will accurately capture minute volume increments in oil saturation within the shale. The second objective is to use NMR spectroscopy as a tool to visualize the saturation

profile of fluids. The last objective is to determine the liquid permeability of the shale during oil intrusion.

The goals of this research were studied by performing forced oil intrusion experiments on crushed shale particles using a slightly compressible mineral oil at various levels of elevated pressures. The pressure response during oil intrusion was analyzed and subsequently, the saturation profile was visualized with the aid of NMR Spectroscopy.

1.3 Overview of Chapters

This report is organized into six chapters.

Chapter 1 reviews the global energy demand and justifies the need to obtain accurate capillary pressure curves and permeability estimate for use in unconventional reservoir simulations.

Chapter 2 provides a holistic description of the theory behind capillary pressure and permeability. It also highlights various methods from previous studies, that have been used to estimate both capillary pressure curves in conventional rocks and permeability in unconventional reservoirs.

Chapter 3 outlines the laboratory procedure for the pressure decay and capillary pressure experiments. It also describes all of the components of the laboratory setup.

Chapter 4 presents graphical plots of pressure decay data obtained during the experiments. It also presents the calculations used in interpreting the data and finally shows the results from the calculations performed on the experimental data collected for permeability measurement and capillary pressure curve estimation.

Chapter 5 discusses Nuclear Magnetic Resonance (NMR) spectroscopy. It explains the governing physics and application with respect to conventional and

unconventional rocks. It also outlines and presents its use in visualizing the fluid distribution within the pore spaces.

Chapter 6 summarizes the key learnings from this research and outlines some recommendations for future work.

Chapter 2: Literature Review

Capillary pressure exists when two or more immiscible fluids are present within tiny pores spaces of reservoir rocks. The magnitude of the capillary pressure between fluid interfaces in a reservoir rock is influenced by; the wettability of the rock (this determines the contact angle between the fluid phases and the rock grain), the interfacial tension between fluid phases present, the extent of saturation of each phase, and the permeability of the rock (Leverett, 1941) and (Bruce & Welge, 1947). For a fluid pair, capillary pressure is defined as the pressure difference between the non-wetting phase and the wetting phase.

$$P_c = P_{nw} - P_w \qquad (2.1)$$

For tight rocks with nanometer-sized pores, the effects of capillary pressure become increasingly important to consider because it affects the initial fluid saturations prior to production and during production.

2.1 PETROPHYSICAL CONCEPTS ON CAPILLARY PRESSURE

The theory on capillary pressure will not be complete without a brief discussion of interfacial tension and wettability. Interfacial tension exists, whenever two or more immiscible fluid phases are present within the pores of reservoir rocks. At the interface between the fluid phases, a surface free energy exists and it follows the principle of energy minimization which states that; systems tend to proceed in the direction that minimizes their free energy. This surface free energy or surface tension is also known as interfacial tension when two or more interfaces coexist. Interfacial tension is defined as the energy stored per unit area across the newly formed boundary between the interfaces of the immiscible fluids in contact.

Consider the system represented below with three phases in equilibrium. Three interfacial forces exist. These are; the interfacial tension between the gas and the liquid, interfacial tension between the gas and the solid and the interfacial tension between the solid and the liquid. A force balance in the x-direction on this system at equilibrium gives;

$$\sigma_{liq-solid} + \sigma_{gas-liq}\cos\theta - \sigma_{gas-solid} = 0 \qquad (2.2)$$

Solving for contact angle in the above equation gives;

$$\cos\theta = \left(\frac{\sigma_{gas-solid}-\sigma_{liq-solid}}{\sigma_{gas-liq}}\right) \qquad (2.3)$$

The above equation is known as the Young – Dupre's equation. The contact angle which is usually measured through the denser phase can be between 0^0 and 180^0. Three scenarios can arise from the above equation.

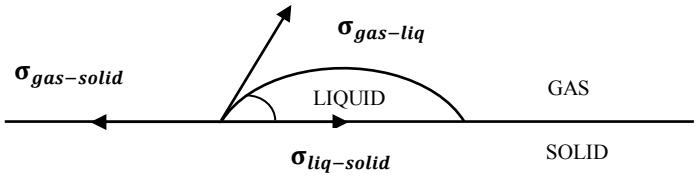

Figure 2.1 Illustration of three interfacial tensions

A contact angle of less than 90^0 implies that the surface energy created by the interface between the gas and solid is greater than that of the liquid – solid interface. Going by the energy minimization principle earlier stated, this implies that the solid phase would prefer to be in contact with the liquid phase because the amount of energy required to form this interface is less. Hence, the liquid phase is referred to as the wetting phase, while the gas is the non-wetting phase.

Conversely, a contact angle of $90^0 \leq \theta \leq 180^0$ implies that the $\sigma_{gas-solid} < \sigma_{liq-solid}$. Thus, the gas phase becomes the wetting phase and the liquid phase is the non-wetting phase. If both the surface energies required to create the gas - solid and liquid – solid interfaces are equal, then the contact angle becomes zero and, in this case, neither the gas nor the liquid phase is preferentially wetting. Thus, the system is said to be in a mixed wet state.

Figure 2.2 Illustration of liquid and gas as wetting phases.

Wettability of core samples can be measured via rate of imbibition tests, adhesion tests and critical disjoining pressure measurements, (Anderson, 1986). Evans and Guerrero, (1979) noted that capillary pressure does not exist as a pressure gradient across a fluid phase, thus, it does not provide the potential gradient to cause fluid phases to flow. However, they noted that when considered on a molecular level, it occurs over the thickness of the molecular interface between two fluids and this molecular interface is almost negligible. They also noted that the capillary pressure is an equilibrium measurement and is a function of radius of curvature as given by the equation below.

$$P_c = \sigma \cos\theta \left(\frac{1}{R_1} + \frac{1}{R_2}\right) \qquad (2.4)$$

Where R_1 and R_2 are the principal radii of curvature, and P_c is the capillary pressure.

2.2 USES OF CAPILLARY PRESSURE CURVES

Capillary pressure curves show the relative sorting of the grains, (Evans and Guerrero, 1979) and this provides an estimate of the pore size distribution within the sample. The capillary pressure curves also allow us to measure the residual oil saturation and the connate water saturation which are essential for developing an efficient tertiary recovery program. Capillary pressure curves have also been used to estimate producible porosity – defined as the pore volume available to hydrocarbon emplacement - when the maximum capillary pressure is calibrated to T_2 relaxation time distribution cut-off obtained via NMR. (Dodge et. al 1996).

The effect of capillary pressure has also been known to affect wellbore stability during drilling in shale reservoirs (Forsans & Schmitt 1994) and capillary pressure curves have been used for the improved prediction of the compressive strength of mud/shale in interaction with reservoir fluids.

Capillary pressure curves can also be used to determine water saturations in hydrocarbon reservoirs in conjunction with resistivity logs (Evans and Guerrero, 1979). Precise capillary pressure curves are required for accurate estimation of phase pressures because at low wetting phase saturation, capillary pressure curves have steep slopes, thus, slight differences in saturation could result in huge discrepancies in capillary pressures.

2.3 STATIC METHODS FOR MEASURING CAPILLARY PRESSURE

Several methods have been proposed to estimate capillary pressure curves in conventional rocks.

They are;

1. Mercury Injection.
2. Porous plate method.
3. Centrifuge method

The mercury injection method is quite fast and reliable, but it is a destructive method because it uses mercury and mercury vapor as the injection fluid. It generates the drainage curve by measuring the amount of mercury that has invaded the sample as the mercury pressure surrounding the sample in the sample chamber is increased. The imbibition curve is obtained by depressurizing the sample chamber and measuring the amount of mercury expelled from the core.

The porous plate method is a time consuming but non-destructive method and it can be used with the actual reservoir oil – brine samples. It makes use of a porous membrane (impermeable to the non-wetting phase) to separate the flow of the non-wetting phase from the wetting phase as drainage occurs. The drainage capillary pressure curve is obtained by measuring the volume of the wetting phase expelled at equilibrium for various pressure increments, until the porous membrane becomes permeable to the non-wetting phase.

The centrifuge method is commonly used because it is fast, non-destructive and can be used with the actual reservoir fluids. This method involves the spinning of a pre-cleaned, wetting phase saturated core, at various centrifugal speeds and recording the volume of wetting fluid expelled at equilibrium. The capillary pressure and wetting phase saturation obtained via this method varies with the distance along the length of the core. As such, the average capillary pressure and wetting phase saturation is obtained by integrating the expression for the difference between the non-wetting phase and wetting phase differential pressures using Hassler's boundary condition. The rotary speed is converted to pressure, and the pressure versus wetting phase saturation is plotted. This method however assumes that the capillary pressure at the outlet end of the core is zero which is not true at high revolutions.

2.4 AGREEMENT BETWEEN STATIC AND DYNAMIC METHODS

Brown, (1951) described all the methods outlined above as static methods. He proposed a dynamic method which involved the simultaneous flow of both the wetting and non-wetting phase across the core while controlling the pressure difference between both phases until equilibrium is achieved with non-changing phase saturations. The pressure difference thus obtained was an indication of the capillary pressure. The dynamic method was proposed because questions had been asked over the validity of the use of capillary pressure curves obtained under static equilibrium as compared to those obtained under dynamic equilibrium, which reflects the actual reservoir state during production. The results from his experiments carried out with two phases (oil and gas) present in a sandstone and limestone core showed that both methods showed almost exact agreement and the use of static capillary pressure data for dynamic systems was indeed valid.

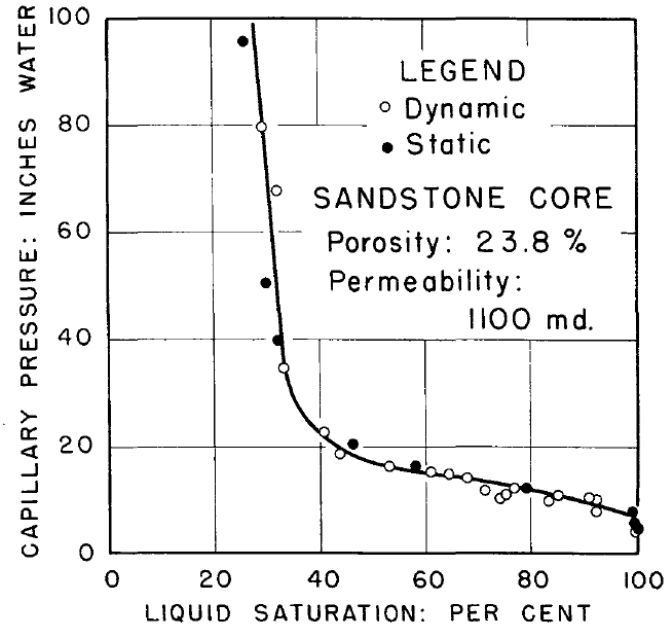

Figure 2.3 Capillary pressure curves by static and dynamic methods in sandstone cores. (Brown 1951)

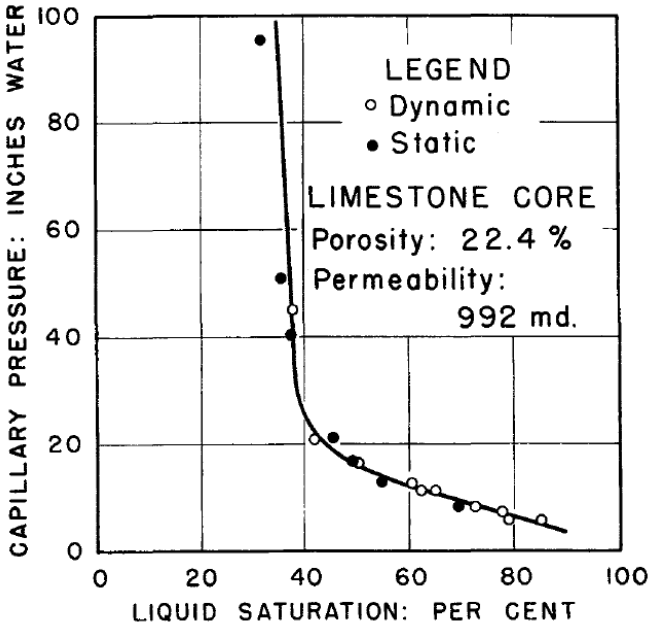

Figure 2.3 Capillary pressure curves by static and dynamic methods in limestone cores. (Brown 1951)

2.6 Effect of Capillary Pressure on Fluid Density and Phase Behavior in Shale

The nature of the pore sizes in shale and tight reservoirs (which is of the order of nanometers) makes capillary pressure effects important. Nojabaei et al (2012), noted that capillary pressure can affect the phase behavior of in-situ reservoir fluids and ignoring its contribution can lead to significant errors in the forecast of ultimate recovery and saturation pressures for the fluid phases in the reservoir. In their research, they combined the effect of capillary pressure with phase equilibrium calculations and solved the resulting non-linear fugacity equations to highlight the effect of capillary pressure on fluid densities and saturation pressure for rocks with very small pore sizes.

Their study noted that capillarity in small pores decreases the bubble point pressure or dew point pressure, depending on which part of the two-phase envelope is being considered. They also pointed out that there could be a reduction in fluid densities

as a result of capillary effect and this could significantly affect the estimates of formation volume factors and ultimate reserve calculations. Overall, the importance of measuring interfacial tension and pore size distribution was highlighted because both of these could impact capillary pressure.

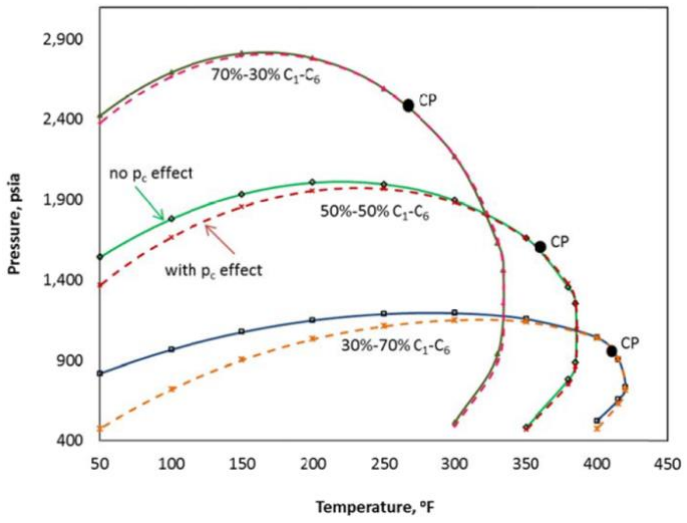

Figure 2.4 Phase envelopes showing the effect of Capillary Pressure for binary mixtures of methane and hexane. (Nojabaei et al, 2012).

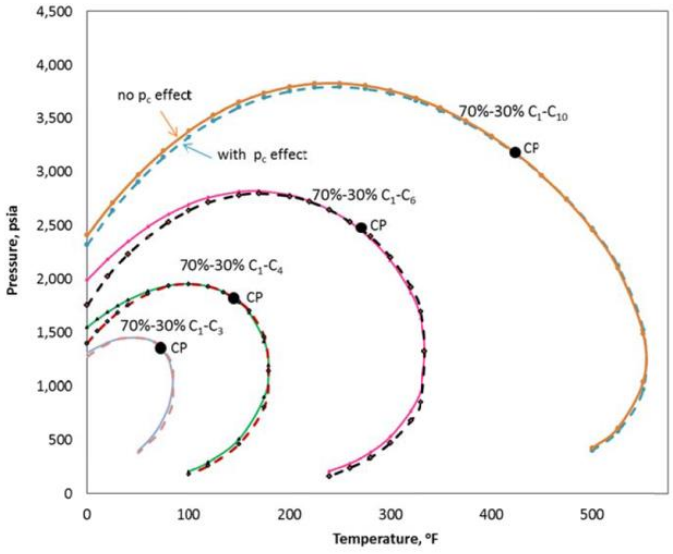

Figure 2.5 Phase envelopes showing the effect of Capillary Pressure for binary mixtures of methane and other alkanes. (Nojabaei et al, 2012).

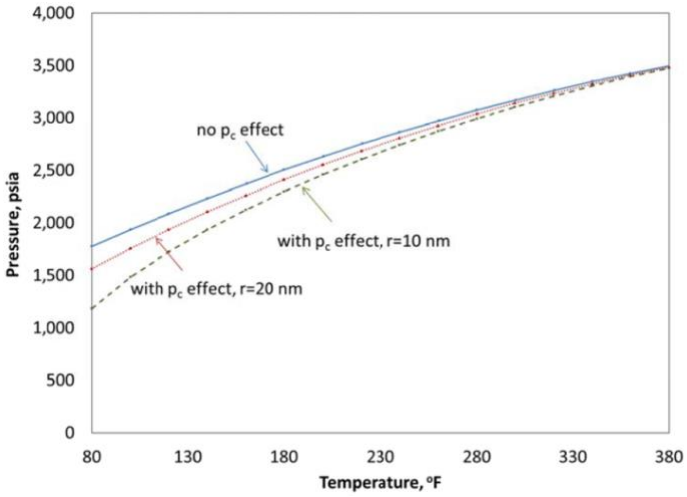

Figure 2.6 Effect of capillary pressure on the bubble point of Bakken oil (Nojabaei et al, 2012).

2.9 PERMEABILITY DETERMINATION

Permeability is an intrinsic rock property. It is a measure of the extent to which a fluid will flow through a porous medium under a pressure gradient (Metwally et al. 2011). Using Darcy's law, the rock's intrinsic permeability can be estimated by measuring the steady state flow rate across a sample subjected to a constant pressure gradient;

$$k = \frac{Q\mu}{A}\left(\frac{dP}{dx}\right)^{-1} \qquad (2.5)$$

Where Q is the volumetric flow rate, k is the permeability, A is the cross-sectional area, μ is the viscosity and $^{dP}/_{dx}$ is the pressure gradient in the axial direction.

There are two broad categories for measuring permeability in shales. They include;

1. Steady state method.
2. Transient method.

2.9.4 Steady State Method

In the steady state method, a net confining stress is applied on the core sample and a constant pressure difference is applied across the core. Thereafter, the fluid flow rate through the core is measured and the permeability is determined using Darcy's Law.

However, due of the 'tightness' of shales, steady-state methods are infrequently used for permeability measurements in tight resources, because these rocks require a longer time to achieve a steady inlet and outlet flow rate. A single test can take months to complete and they require a high level of precision to measure extremely low flow rates. (Cui et al, 2009).

2.9.5 Transient Methods

Transient methods of determining permeability rely on measuring the decay or growth in pressure imposed on the sample instead of flow rate or flow velocity measurements across the sample as is the case for steady state methods. Also, recent technological advancement in data-acquisition and precise pressure transducers have made it possible to carry out permeability measurements in the laboratory under transient state conditions. Several transient methods have been applied and a few of the them are mentioned briefly below.

2.9.5.1 Pulse decay method for core plugs

The pulse decay method involves measuring the reduction in the upstream pressure and increase in downstream pressure induced as an inert gas flows through a core plug placed between two reservoirs with the aid of two pressure transducers. One transducer measures the differential pressure between both reservoirs, the other measures the absolute pressure of the downstream reservoir and the upstream pressure is obtained by summing the differential and downstream pressure. The dimensionless differential

pressure obtained using the expression below, can be plotted logarithmically against time to obtain a straight line. The governing equation for the pulse decay method is obtained from the differential equation for one-dimensional linear flow of a compressible fluid through a medium (Brace et al., 1968).

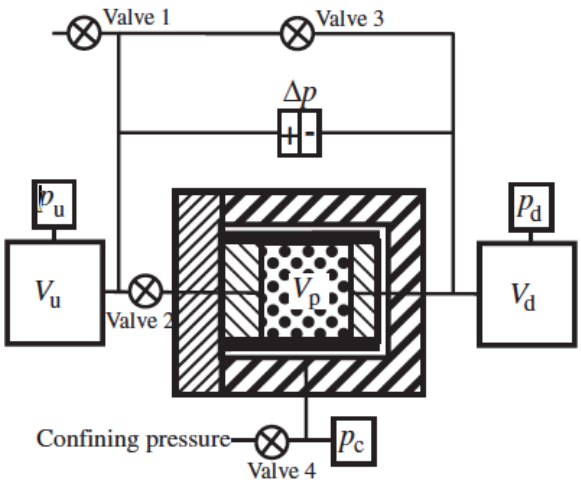

Figure 2.7 Schematic diagram of a typical pulse decay apparatus. (Cui et al. 2009)

Based on an analysis of the equation that describes the pressure change during the experiment, the slope of the straight line can be used in conjunction with known experimental parameters to calculate the plug's permeability.

2.9.5.2 Pressure build-up method

This method is similar to the pulse decay method. However, it implements a technique that senses more of the sample. This method creates an infinite storage capacity for the upstream reservoir by keeping its pressure constant. The implication is that the initial pressure difference decays only after the pressure change is felt at the other end of the sample. The constant pressure in the upstream reservoir eliminates the permeability

error associated with the neglect of adsorption, neglect of absolute upstream reservoir volume and leaks, (Metwally et al. 2011). This experiment can be conducted at reservoir conditions on a directionally cored core sample rather than crushed samples.

2.9.5.3 Permeability on crushed samples

Crushed shale permeability can be determined during a gas expansion experiment to estimate porosity, (Cui et al 2009). The procedure uses an inert gas whose pressure is equilibrated both in the sample and reference chamber just before the gas pressure is increased in the sample chamber. The pressure in the sample chamber declines as the gas diffuses into the pores and gradually reaches an equilibrium pressure.

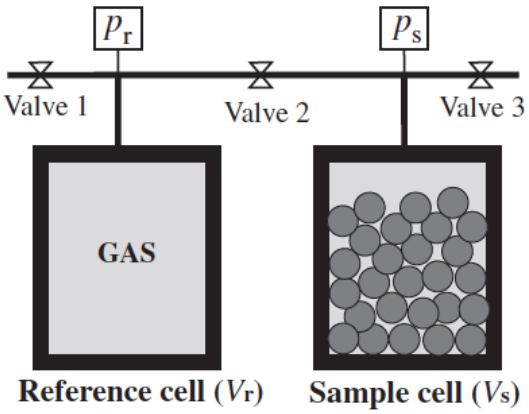

Figure 2.8 Schematic diagram of a pycnometer apparatus. (Cui et al. 2009)

The time-dependent pressure decay data can be analyzed based on the equation governing the pressure diffusivity within the crushed particle. Based on this analysis, an early time or late time approach can be adopted to determine the permeability of the crushed shale particles. The late time approach however is preferred because the early time approach can only match the exact solution at very small times if the ratio of the pore volume to the sample chamber volume is very large (Cui et al. 2009).

Chapter 3: Experimental Apparatus and Procedures

3.1 Experimental Procedure for the Oil Saturation Experiments

Determination of capillary pressure curves in tight oil reservoirs involves careful estimation of changes in oil saturation during forced imbibition, because only very minute volumes of oil can be pushed through the shale matrix even at high pressure owing to the extremely low permeability of these mudrocks. Thus, a novel method of measuring such tiny increments in saturation had to be employed. The use of pressure decay data, provided a way by which these incremental saturations could be measured.

The following paragraphs describes the experimental procedure adopted for this proposed method of determining capillary pressures as well as liquid permeability in shale.

3.2 Crushed Shale Preparation

Bulk samples of unpreserved Eagle Ford outcrop were selected from the mudrock repository within the research group. These samples were crushed using a mortar and pestle in the coring laboratory and sieved to mesh sizes between +10 to +20 (0.841 - 2mm) and +5 to +10 (2 – 4mm) respectively. The crushed particles from both sample sizes were weighed and stored in separate glass bottles for sample preservation. These glass bottles were placed in a vacuum oven with their lid open for 24 hours at 100^{o}C. After vacuuming and drying, the lids were replaced and each bottle was left to cool before re-weighing. The weight before and after drying was used to calculate the percentage of fluid vaporized.

3.3 Fluid Preparation

A known volume (about 300 ml) of mineral oil is charged into one end of the accumulator while water – which serves as the driving fluid - is filled into the other end

of the accumulator that is connected to the pump outlet. For the accumulator containing confining oil, machine oil was charge in at the end connected to the hydraulic pump and served as the driving fluid, while confining oil filled the other end of the accumulator that was connected to the core holder.

3.4 CORE HOLDER PREPARATION

A specified amount of the crushed shale particles (approximately 21.50g) with particle size ranging between 2 – 4mm in diameter was loaded into the sample chamber of the core holder. The sample chamber consisted of a hollow cylindrical ULTEM™ plastic container which served as confinement for the crushed particles. Shrink tubing was used to securely fasten the distribution plugs of the core holder to the crushed shale and ULTEM™ plastic assembly. The annular space within the core holder was initially filled with confining oil at atmospheric pressure.

3.5 SPONTANEOUS IMBIBITION PROCEDURE

A spontaneous imbibition test was firstly carried out to determine the wettability of the shale. The procedure is given below;

Crushed shale sample of mesh size 5 - 10 is oven dried at 100^{o}C for 24 hours to reduce any residual water saturation. After oven drying, the sample is vacuumed for 12 hours to eliminate any trapped air within the pore spaces. After vacuuming, 30 grams of the crushed sample is weighed into a beaker containing 200ml of freshly distilled water.

The beaker containing the shale sample is left to stand for 72 hours, after which it is emptied and the sample is retrieved. The sample is subsequently dried and re-weighed to estimate the amount of water imbibed. Afterwards, an NMR T_2 scan is performed to visualize the extent of imbibition and to see what pore size ranges imbibed the most water.

3.6 CAPILLARY PRESSURE AND PERMEABILITY EXPERIMENTAL PROCEDURE

Crushed shale sample of mesh size 5 - 10 is oven dried at 100^{o}C for 24 hours to reduce any residual water saturation. After oven drying, about 21.5 grams is weighed into the sample chamber of the core holder. The core holder is then assembled and filled with confining oil at atmospheric pressure.

The setup is vacuumed for 12 hours to eliminate any trapped air within the sample chamber and the pore spaces of the shale. After vacuuming, the sample chamber is filled with dodecane and pressurized to a constant pressure of 50 psi after which it is left to equilibrate for about 24 hours. Subsequently, the dodecane pressure within the sample chamber is increased to 100psi for about 5 minutes to allow the pressure transmit uniformly within the bulk fluid phase in the sample chamber before the pump is switched off and the bypass valve on the oil side of the accumulator is closed.

The subsequent pressure decay within the sample chamber is recorded over a period of time, till an equilibrium pressure is reached, where the pressure remains constant and no longer declines. The dodecane pressure is increased to 200psi, 500psi, 1000psi, 2000psi, 3000psi and 4000psi respectively. Each time, a 5-minute wait period is observed for pressure pulse stabilization within the sample chamber, before the accumulator bypass valve is shut and pressure versus time data recorded, until the equilibrium pressure for each initial pressure is reached.

3.7 PROCEDURE FOR THE NMR EXPERIMENTS

Crushed shale of mesh size 5 - 10 is oven dried vacuumed at 100^{o}C for 12 - 24 hours to reduce any residual water saturation. Afterwards, about 21.5 grams of the sample is weighed into a metal tea strainer, and immersed into an accumulator that is filled on one side with dodecane and on the other side with water. The accumulator is pressurized to 500 psi for about 24 hours and thereafter, depressurized so the metal tea strainer

containing the shale sample can be retrieved. After retrieval, the tea strainer is placed in a fume cupboard for about 20 minutes to dry the dodecane on the surface of the shale particles. Then, the particles are emptied into a glass bottle and inserted into the NMR spectrometer, where a T_2 scan is carried out to visualize the extent of oil intrusion and to see what pore size ranges are being saturated with oil. The same procedure is repeated at oil pressures of 2000psi and 4000psi.

3.8 DESCRIPTION OF EXPERIMENTAL APPARATUS

A description and specification of each component used in the experiment is given below.

3.8.1 Pumps

Three different types of pumps were used for this experimental study. Hydraulic pump, vacuum pump and a continuous flow syringe pump.

3.8.1.1 Hydraulic pump

An Enerpac P-391 hydraulic pump was used to pump the confining oil into annular space within the core holder to provide overburden pressure. The pump is rated for a maximum pressure of 10000 psi.

3.8.1.2 Vacuum Pump

A Welch Duo Seal vacuum pump with ultimate vacuum of 0.00002psi and free air displacement of 160 liters/min at 60Hz was used to induce a vacuum within the sample chamber in the core holder. It was also used to remove any trapped gas within the shale matrix, prior to oil saturation.

3.8.1.3 Continuous flow pump

A QX-6000 Series Pump made by chandler engineering and comprising of two independent positive displacement pump cylinders, capable of delivering or receiving fluid was used to inject mineral oil and maintain a constant pressure during oil saturation within the core holder. The pump has a maximum delivery pressure of 6000psi and a maximum flowrate of 50ml/min with an accuracy of 0.1%. Shop air at 90psi was supplied to the instrument lines of the pump to actuate its syringe.

3.8.2 Valves

Several Swagelok and Autoclave stainless steel valves were used to isolate lines, set flow paths and control pressure. The Swagelok valves were rated for pressure up to 2500psi, while the Autoclave valves were rated for pressures up to 15000psi.

3.8.3 Tubing

Stainless steel 1/8-inch tubing was used as conduit for all flow lines, with the exception of the vacuum pump, which made use of 1/4-inch plastic tubing. The 1/8-inch tubing was rated for pressures up to 10,200 psi. While the 1/4-inch tubing was rated for pressures up to 400 psi.

3.8.4 Pressure Indicator and Transducer

3.8.4.1 Gauge Pressure Indicator

An analog pressure indicator was used to monitor the overburden pressure supplied by the hydraulic pump on the confining oil line leading to the core holder. The gauge has a range of 0 -10,000 psi.

3.8.4.2 Differential Pressure Transducer

Two Rosemount model 3051CD differential pressure transducers, capable of measuring differential pressure in the range from 0 – 300 psi and with an accuracy of 0.1%, were used to measure the pressure difference between the oil outlet on the accumulator and the oil pressure within the sample chamber of the core holder.

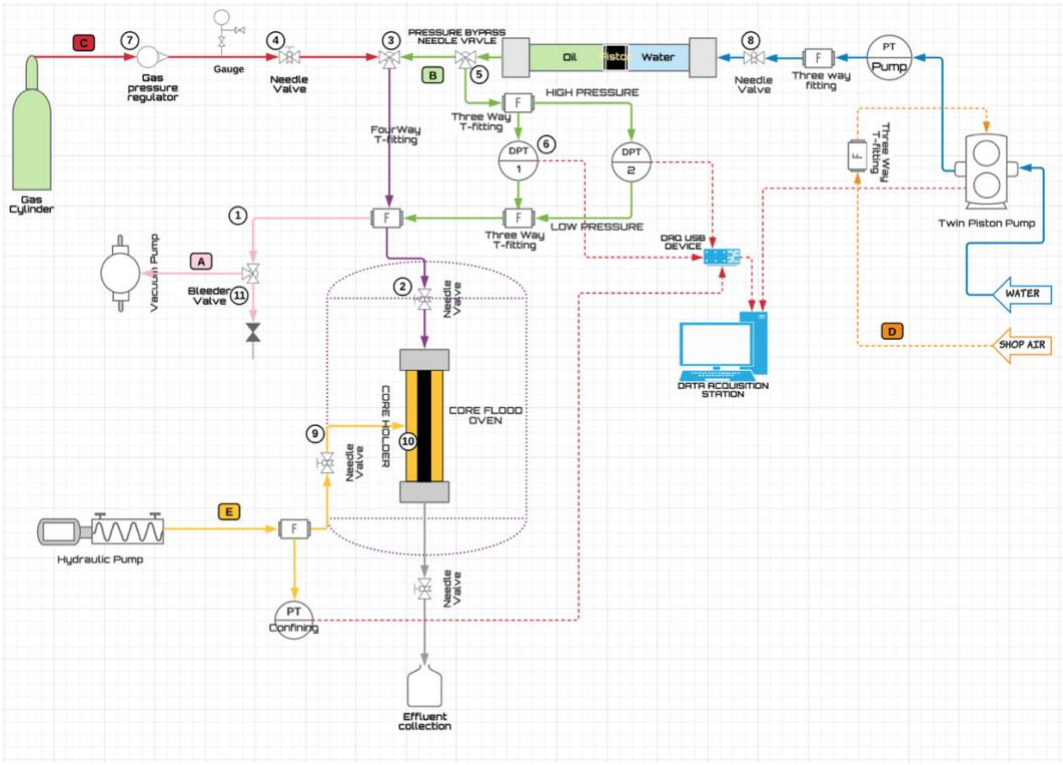

Illustration 3.1 Process flow schematic for the permeability and capillary pressure experiments.

3.8.5 Accumulators

Three stainless steel accumulators with capacities of 500 cc and 1,000 cc were used for this experiment. Two of the accumulators contained water and mineral oil (dodecane), while the other accumulator contained machine oil and the confining oil (a Perfluoro-compound with trade mark name FC-40TM). Each accumulator contained two

liquids and a piston was used to separate both liquids within each accumulator. The piston was made from PEEK (polyether ether ketone), and it had Viton O-rings to enable it serve as a good seal. The accumulators were rated for a maximum pressure of 5,000 psi at temperature of 350oF.

3.8.6 Weighing Balance

A top-loading balance from Mettler Toledo with a maximum load of 120g and an accuracy of 0.1mg was used for weighing the crushed shale sample before and after final saturation at 4,000 psi.

3.8.7 Computer Software

Quizix Pumpworks software was used to interface and operate the Quizix Pump, while LabVIEW was used for data acquisition. Both pieces of software were installed on a Dell laptop (model PSW390) running an Intel® Core TM IV processor. The software was used to define operating modes, set pump pressures, setup data logs and adjust other pump parameters.

3.8.8 Core Holder

A Fiberglass body style FCH 1.0 composite core holder from Core Laboratories, compatible with NMR, microwave, x-ray, and gamma ray imaging was used for this experiment. The FCH body style core holder is a biaxial-type core holder and it is capable of applying a common radial and axial overburden stress to the crushed shale sample. It has a maximum working pressure of 5000psi at a working temperature of 300oF. The core holder can accommodate core plugs of one-inch diameter and up to three-inch in length. The crushed shale particle was contained within an ULTEM^{TM} plastic hollow cylindrical container and shrink tubing was used to wrap the plastic tightly to the distribution plugs within the core holder.

3.8.9 NMR Spectrometer

A GEOSPEC 2-53, Oxford Instruments Magnetic Resonance rock core analyzer with 2MHz Larmor frequency was used for the magnetic resonance imaging. The magnetic unit consist of a magnet with 0.046T magnetic field strength, a probe, gradient coils, pre-amplifier and a recirculation chiller. The machine operates at temperatures between 19^{o}C and 25^{o}C.

3.8.10 Air dehumidifying unit

A TNB model W80 air unit was used. The unit had an air filter, an oil filter and a dehumidifier to remove moisture from the air before going into the pump's instrument line. Air was supplied to the pump at 90psi from the mains supply.

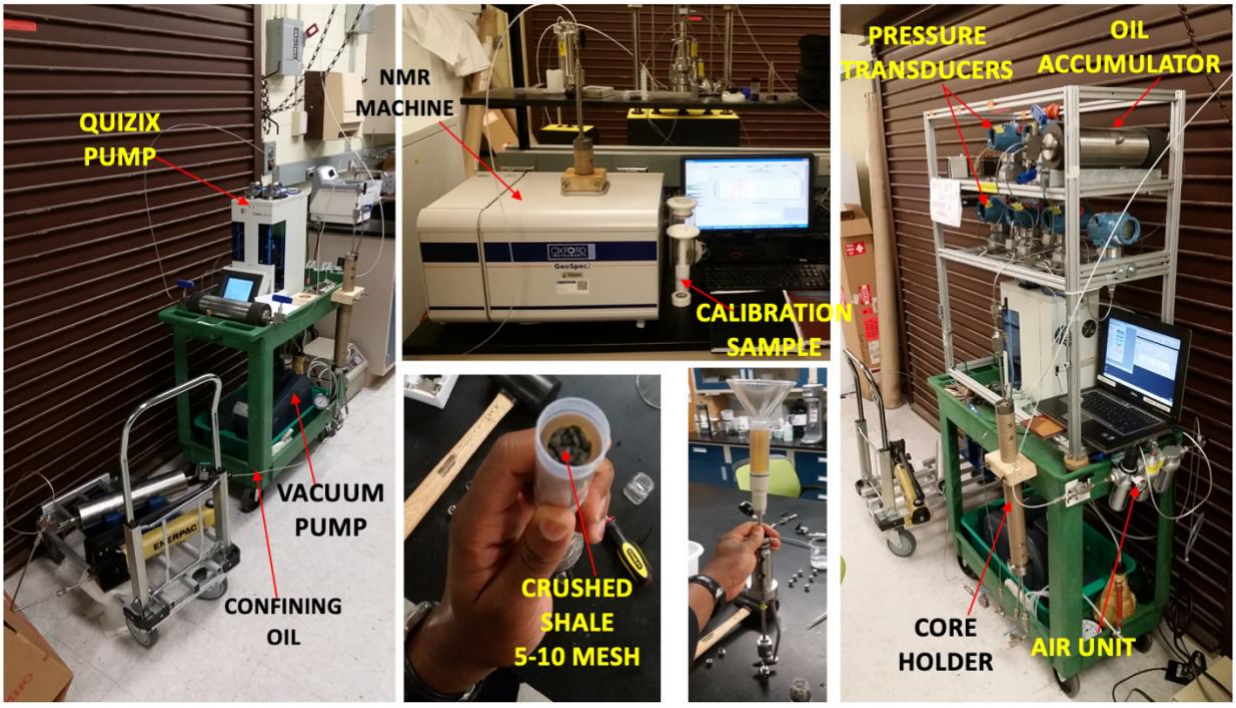

Illustration 3.2 Laboratory setup for the permeability and capillary pressure experiments.

Chapter 4: Permeability and Capillary Pressure Estimates in Tight Rocks

4.1 THEORETICAL BASIS FOR THE CRUSHED SHALE PERMEABILITY SOLUTION.

The continuity equation (without adsorption) for radial fluid flow only in a porous spherical particle is given as (Bird et al., 2007);

$$\frac{\partial}{\partial t}(\rho\phi) + \frac{1}{r^2}\frac{\partial}{\partial r}(\rho r^2 v_r) = 0 \qquad (4.1)$$

For creeping flow in a porous medium, Darcy's law can be assumed for the superficial velocity in the radial direction.

$$v_r = -\frac{k}{\mu}\frac{\partial P_s}{\partial r} \qquad (4.2)$$

Substituting Darcy's Law into the continuity equation and after some algebra the Radial Diffusivity equation is obtained.

$$\frac{\partial P_s}{\partial t} = \left(\frac{k}{\mu c_0 \phi}\right)\frac{1}{r^2}\frac{\partial}{\partial r}\left(r^2\frac{\partial P_s}{\partial r}\right) \qquad (4.3)$$

$$\frac{\partial P_s}{\partial t} = \kappa\frac{1}{r^2}\frac{\partial}{\partial r}\left(r^2\frac{\partial P_s}{\partial r}\right) \qquad (4.4)$$

The pressure transport coefficient, κ can be defined as follows;

$$\kappa = \left(\frac{k}{\mu c_o \phi}\right) \qquad (4.5)$$

Thus, the PDE becomes

$$\frac{\partial P_s}{\partial t} = \kappa\frac{1}{r^2}\frac{\partial}{\partial r}\left(r^2\frac{\partial P_s}{\partial r}\right) \qquad (4.6)$$

The following initial and boundary conditions apply to this specific problem;

Initial Condition

$$P_s(r, 0) = P_i(r) \qquad (4.7)$$

Boundary Conditions

1. Symmetry about the center of the sphere.

$$\left.\frac{\partial P_s}{\partial r}\right|_{r=0,t} = 0 \qquad (4.8)$$

2. Mass Balance Condition

The solution to the above differential equation must also satisfy the mass balance condition that states that the radial flowrate out of the sphere is determined by the rate of pressure decay within the bulk fluid. Mathematically,

$$(4\pi r^2 N)\frac{k}{\mu}\frac{\partial P_s}{\partial r}\Big|_{r=R,t} = c_o V_o \frac{\partial P_o}{\partial t} \qquad (4.9)$$

$$N = \frac{3M_s}{4\pi R^3 \rho_b} \qquad (4.10)$$

Where N is the total count of spherical shale particles.

The solution to the radial diffusivity equation with the initial and boundary conditions given above is (Carslaw & Jaeger, 1959);

$$P_s(r,t) = \frac{P_i}{\beta+1} - \frac{2\beta R P_i}{3r}\sum_{n=1}^{\infty} e^{-\kappa\propto_n^2 t}\left[\frac{\beta^2R^4\alpha_n^4+3(2\beta+3)R^2\alpha_n^2+9}{\beta^2R^4\alpha_n^4+9(\beta+1)R^2\alpha_n^2}\right](sin\, r\alpha_n\, sin\, R\alpha_n)$$

(4.11)

The solution above is simplified to obtain the pressure at the solid-liquid interface;

$$P_s|_{r=R,t} = P_o(t) = P_o|_{t=0} - \left\{\frac{(P_0-P_i)}{\beta+1} - 6\beta(P_0-P_i)\sum_{n=1}^{\infty} e^{-\kappa\propto_n^2 t}\left[\frac{1}{\beta^2R^2\alpha_n^2+9(\beta+1)}\right]\right\}$$

(4.12)

If we substitute;

$$\alpha = \frac{\lambda}{R} \qquad (4.13)$$

$$P_s|_{r=R,t} = P_o(t) = P_o|_{t=0} - \left\{\frac{(P_0-P_i)}{\beta+1} - 6\beta(P_0-P_i)\sum_{n=1}^{\infty} e^{-\left(\frac{\kappa\lambda_n^2}{R^2}\right)t}\left[\frac{1}{\beta^2\lambda_n^2+9(\beta+1)}\right]\right\}$$

(4.14)

And the transcendental becomes;

$$tan\,\lambda = \frac{3\lambda}{3+\beta\lambda^2} \qquad (4.15)$$

The storage ratio of oil within the shale is given as;

$$\beta = \frac{\rho_b V_o}{\phi M_s} \qquad (4.16)$$

Using the first root of the transcendental equation, the solution can be rearranged to obtain

$$ln\left[\frac{(P_s-P_o)(\beta+1)+(P_0-P_i)}{6\beta(P_0-P_i)(\beta+1)}\right] = -\left(\frac{\kappa\lambda_1^2}{R^2}\right)t - ln\left(\beta^2\lambda_1^2 + 9(\beta+1)\right) \qquad (4.17)$$

A plot of $\ln\left[\frac{(P_s-P_o)(\beta+1)+(P_0-P_i)}{6\beta(\beta+1)(P_0-P_i)}\right]$ versus elapsed time, t would yield a straight line with a negative slope and negative intercept. The slope is given by this expression.

$$slope, m = \left(\frac{\kappa\lambda_1^2}{R^2}\right) \qquad (4.18)$$

The permeability can thus be calculated from the slope as follows

$$m = \left(\frac{k\lambda_1^2}{\mu c_o \phi R^2}\right) \qquad (4.19)$$

Therefore,

$$k = \left(\frac{m\mu c_o \phi R^2}{\lambda_1^2}\right) \qquad (4.20)$$

The experimental parameters used for the permeability and capillary pressure experiments are as follows;

4.2 RESULTS FROM THE PERMEABILITY EXPERIMENT

Parameter	Value
Oil Volume $V_o(m^3)$	15×10^{-6}
Bulk density $\rho_b(\frac{kg}{m^3})$	2456.6
Porosity $\phi(\%)$	8.93
Mass of shale $M_s(kg)$	21.5×10^{-3}
Mean particle radius $R(m)$	3×10^{-3}
Initial Shale Pressure $P_i(Mpa)$	6.72
Initial Oil Pressure $P_o(Mpa)$	13.79
Oil Compressibility $c_o(MPa^{-1})$	0.835×10^{-3}
Oil Viscosity $\mu(Pa.s)$	1.36×10^{-3}

Table 4.1 Experimental parameters.

The Pressure-Time data obtained are presented below.

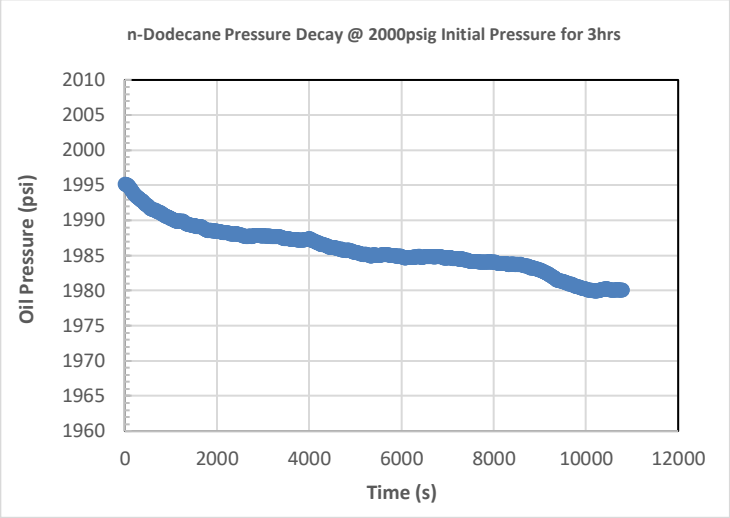

Figure 4.1 Pressure time decay data at 2000 psig

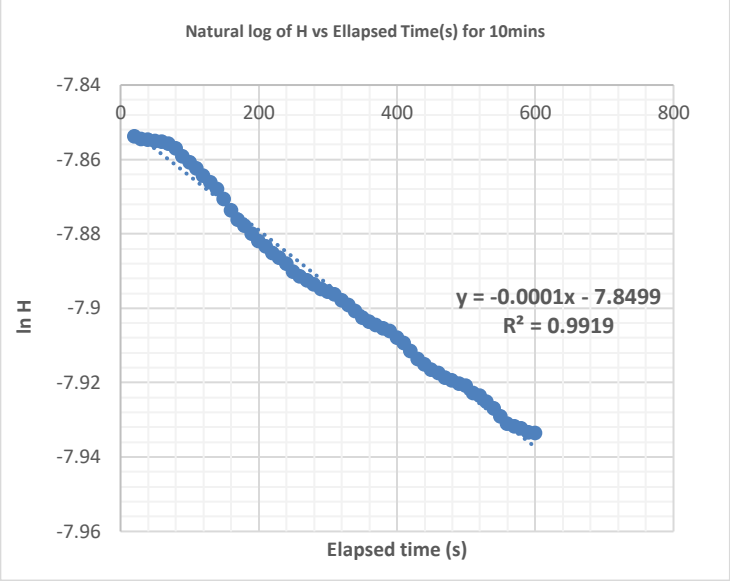

Figure 4.2 Pressure time decay data at 100 psig and ln $\left[\frac{(P_s-P_o)(\beta+1)+(P_0-P_i)}{6\beta(\beta+1)(P_0-P_i)}\right]$ vs time

4.3 THEORETICAL BASIS FOR THE CAPILLARY PRESSURE CURVE ESTIMATION.

Recall that the compressibility of a liquid is given as;

$$c_o = -\frac{1}{V_o}\frac{\partial V_o}{\partial P} \tag{4.21}$$

Thus, the flowrate of the liquid can be derived.

$$c_o V_o \frac{\partial P}{\partial t} = -\frac{\partial V_o}{\partial t} \tag{4.22}$$

The incremental volume can be written as,

$$\Delta V_o = -c_o V_o \int_{t_o}^{t_f} \frac{\partial P}{\partial t} dt \tag{4.23}$$

Where, P is the pressure within each crushed shale particle, V_o is the initial oil volume in the sample chamber, c_0 is the oil compressibility and ΔV_o is the incremental oil volume entering the shale pores. The integral expression in the equation above can be obtained by plotting and curve-fitting the pressure – time series obtained during the experiment. Afterwards, the volume increase at each pressure of oil intrusion during the drainage phase, can be calculated using the expression above and oil saturation can be calculated by dividing the result by the pore volume. The same procedure will be repeated for the imbibition curve. However, this time, a pressure increase with time will be observed within the sample chamber, because as the sample chamber is depressurized, oil will escape from the pore spaces and this will increase the pressure within the chamber.

4.4 RESULTS FROM THE CAPILLARY PRESSURE EXPERIMENT

Initial experiments carried out to determine the capillary pressure curve in shale showed that a careful interpretation and analysis of the pressure - time series obtained during the experiment, could be useful in determining small changes in fluid saturation. The parameters outlined in Table 1 was also used for these experiments, while pump pressure was varied from 100, 200, 500, 1000, 2,000, 3,000 to 4,000 psi. The core holder used had a limiting working pressure of 5,000 psi, hence, pump pressures during the

experiment could not be increased beyond 4,000 psi because a 500 psi excess pressure had to be maintained on the confining oil line. Slight pressure fluctuations were observed within the sample chamber of the core holder as pressure decayed over time. These pressure oscillations could be attributed to temperature variations and uneven pressure transmission within the core holder. To eliminate these pressure fluctuations, a modification to the experimental setup is proposed. The core holder will be replaced with a pressure vessel that is capable of withstanding pressures up to 12,000 psi, thus, higher capillary pressures can be attained and a more comprehensive capillary pressure curve for drainage and imbibition can be obtained. In addition, the pressure vessel will be insulated, in order to eliminate inconsistencies arising from thermal fluctuations.

The pressure time data from the experiment is curve fitted to obtain the integral in equation. This integral is then used as outlined in equation 4.23 to compute the volume increments.

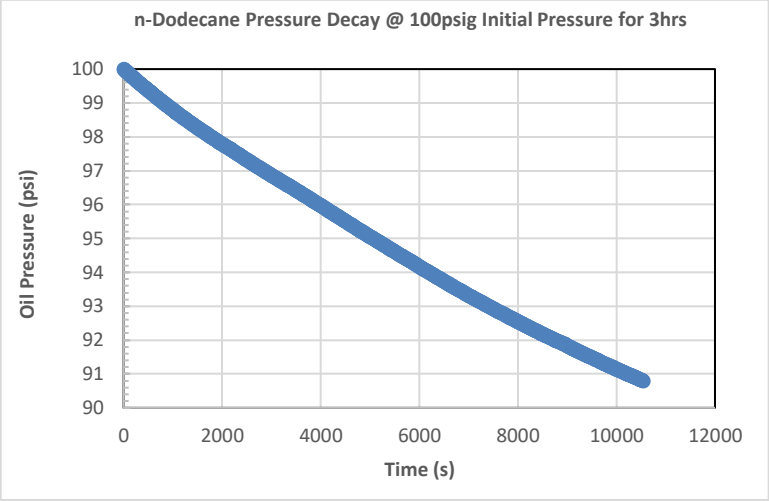

Figure 4.3 Pressure time decay data at 100 psi initial pressure

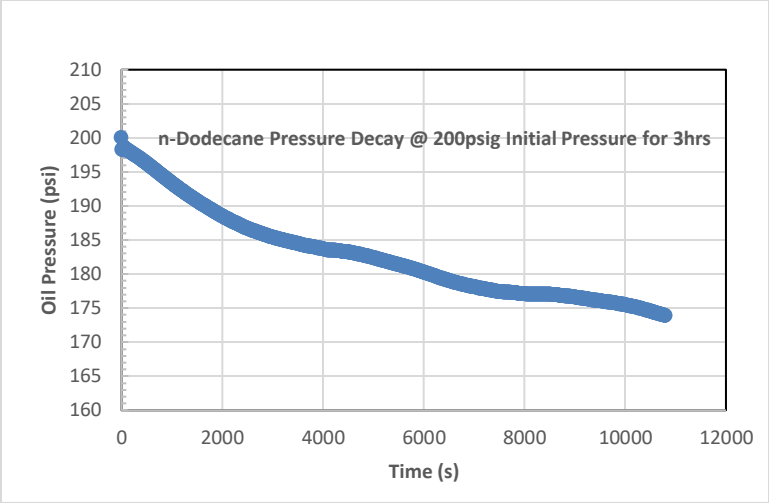

Figure 4.4 Pressure time decay data at 200 psi initial pressure

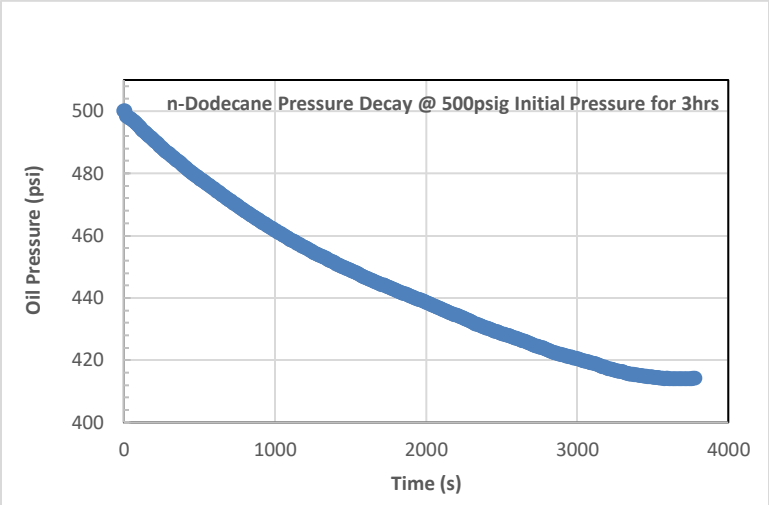

Figure 4.5 Pressure time decay data at 500 psi initial pressure

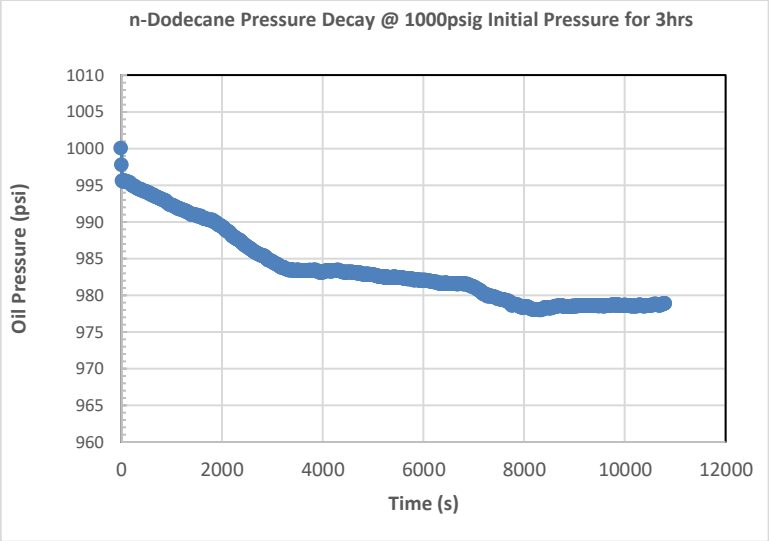

Figure 4.6 Pressure time decay data at 1000 psi initial pressure

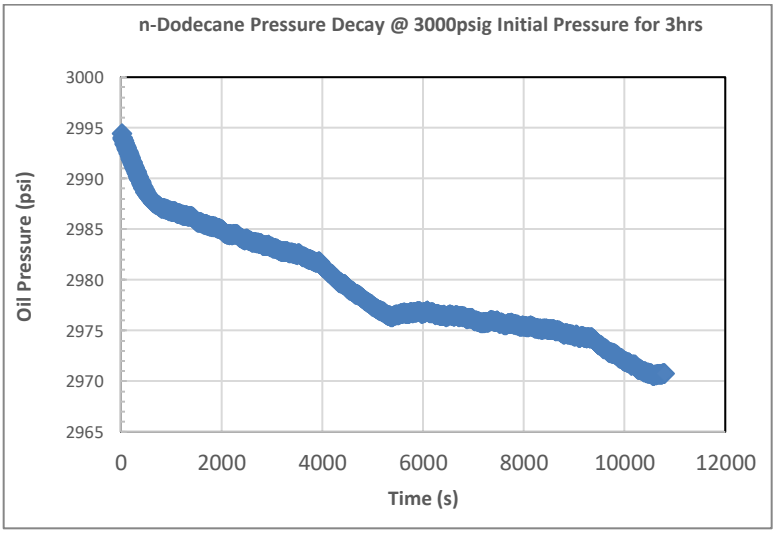

Figure 4.7 Pressure time decay data at 3000 psi initial pressure

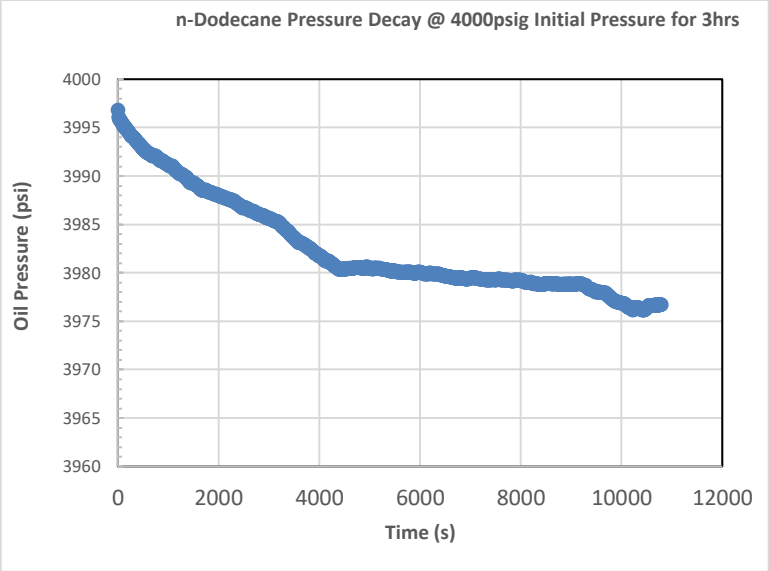

Figure 4.8 Pressure time decay data at 4000 psi initial pressure

The table below was generated for the increase in oil saturation with pressure and the figure below shows drainage capillary pressure curve.

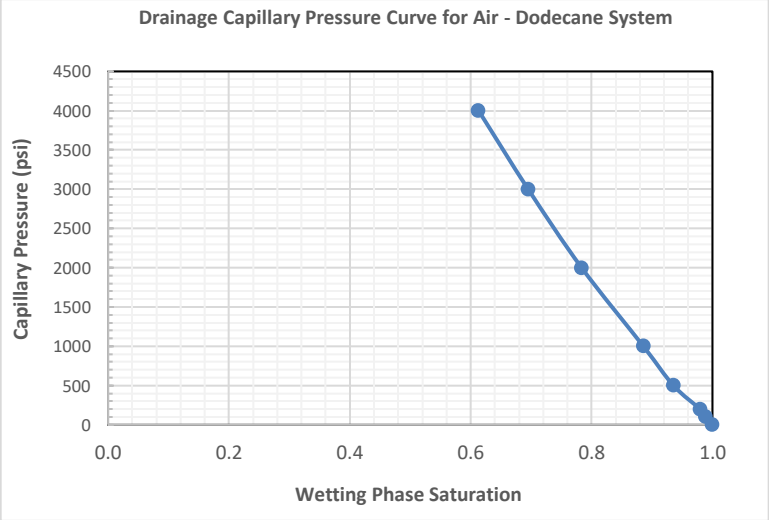

Figure 4.9 Drainage capillary pressure curve.

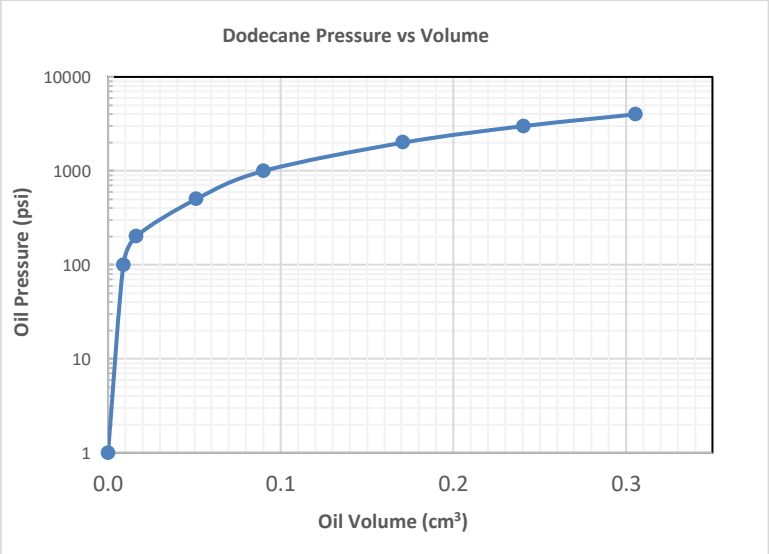

Figure 4.10 Oil volume increments.

Pressure (psi)	**Pressure** (MPa)	**Oil Comp** (MPa^{-1})	**Oil Volume** (cm^3)	**Oil Saturation**	**Wetting Phase Sat**	**Permeability**(nD)
1	0.0069		0	0	1	-
100	0.69	9.49E-04	0.0089	0.0113	0.9887	-
200	1.38	9.42E-04	0.0163	0.0206	0.9794	-
500	3.45	9.22E-04	0.0510	0.0645	0.9355	-
1000	6.89	8.90E-04	0.0902	0.1142	0.8858	39.4
2000	13.79	8.35E-04	0.1710	0.2164	0.7836	36.9
3000	20.68	7.84E-04	0.2409	0.3049	0.6951	34.7
4000	27.58	7.43E-04	0.3056	0.3869	0.6131	32.9

Table 4.2 Results from the capillary pressure curve experiment.

Chapter 5: Fluid Distribution using NMR Spectroscopy

Atoms possess electrons that spin in orbit around the nucleus and protons that also spin within the atomic nuclei. These charged atomic constituents have a magnetic moment and an angular momentum associated with their spins. The spinning of these charged particles gives rise to an electric current which produces a magnetic field perpendicular to the direction of the current. This magnetic field has a magnetic dipole moment associated with it as a result of the direction of its spin. This dipole moment has the ability to produce a magnetic torque when it is placed under the influence of an external magnetic field. The torque generated under an external magnetic field produces a longitudinal angular displacement, which when coupled with the angular momentum, causes the spins to precess about the longitudinal axis of the applied external magnetic field. This precession occurs at a particular frequency known as the Larmor frequency. The Larmor frequency is significant because magnetic nuclei or electrons can only exchange energy at this frequency. This is therefore, the frequency at which magnetic resonance can occur for a proton or an electron and it is at this frequency for a particular atom, that proton nuclear magnetism is studied.

5.1 Longitudinal Relaxation

At ground state, that is in the absence of an external magnetic field, the proton spin of the magnetic nuclei is random, this results in a net magnetization of zero. However, as an external static magnetic field is applied, in the longitudinal direction, a redistribution of nuclei energy occurs, with higher energy nuclei emitting some quantum of energy to its neighboring molecules, thus transiting to a lower energy state, while nuclei of lower energy move to high energy states by absorbing energy from these neighboring molecules. As time progresses, the net magnetization of the system in the

longitudinal direction M_z, builds up to its thermal equilibrium value M_o. Longitudinal relaxation is also known as spin-lattice relaxation because it involves the exchange of energy between the spin of the magnetic nuclei in interaction with molecules within its surrounding lattice.

The following equation is obtained for a magnetization growth curve when the static magnetic field in the longitudinal direction is turned on;

$$M_z^* = M_o\left(1 - e^{-\frac{t^*}{T_1}}\right) \qquad (5.1)$$

The time constant T_1, associated with this process is called the longitudinal or spin-lattice relaxation time. It is the time taken for the magnetization to build up to 63% of its final value (Coates, 1997) and it is indicative of the exchange of magnetic energy between the nuclei spin system and the surrounding lattice. Typically, large values of T_1 reflect little interaction between the nuclei and its lattice, while small T_1 values indicate a significant amount of spin-lattice interaction.

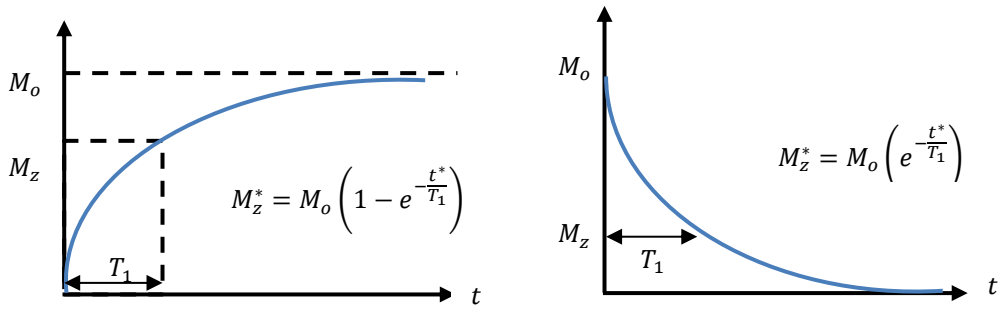

Figure 5.1 Longitudinal relaxation growth and decay curves. (Dunn et al. 2002)

5.1.1 Inversion Recovery

One notable way in which T_1 measurements are carried out is through inversion recovery. This process entails the application of 180^0 pulse to invert the net magnetization vector from the positive to the negative *z* axis followed by the application of a 90^0 pulse after a certain 'recovery' period. The purpose of the 90^0 pulse is to tilt the net magnetization which is an entirely longitudinal vector (with no transverse component) unto the *xy* plane of the receiving coil, so that its signal can be measured. A typical inversion recovery sequence carried out at 0, t_1, t_2, t_3, t_4, is shown below. The value of T_1 can be obtained by fitting the data to a curve given by the equation,

$$M_0(t) = M_o\left(1 - 2e^{-\frac{t}{T_1}}\right) \qquad (5.2)$$

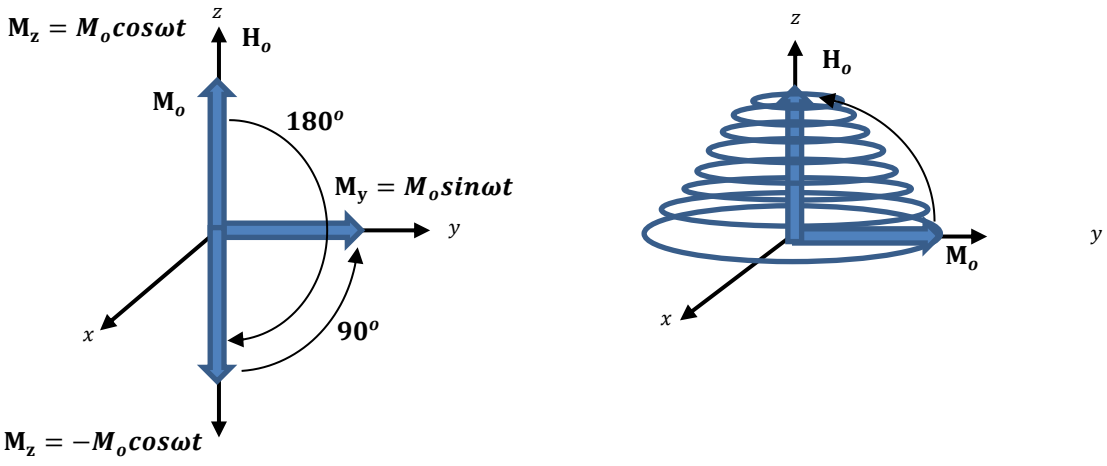

Figure 5.2 Inversion and tilting using 180^0 and 90^0 pulses. (Dunn et al. 2002)

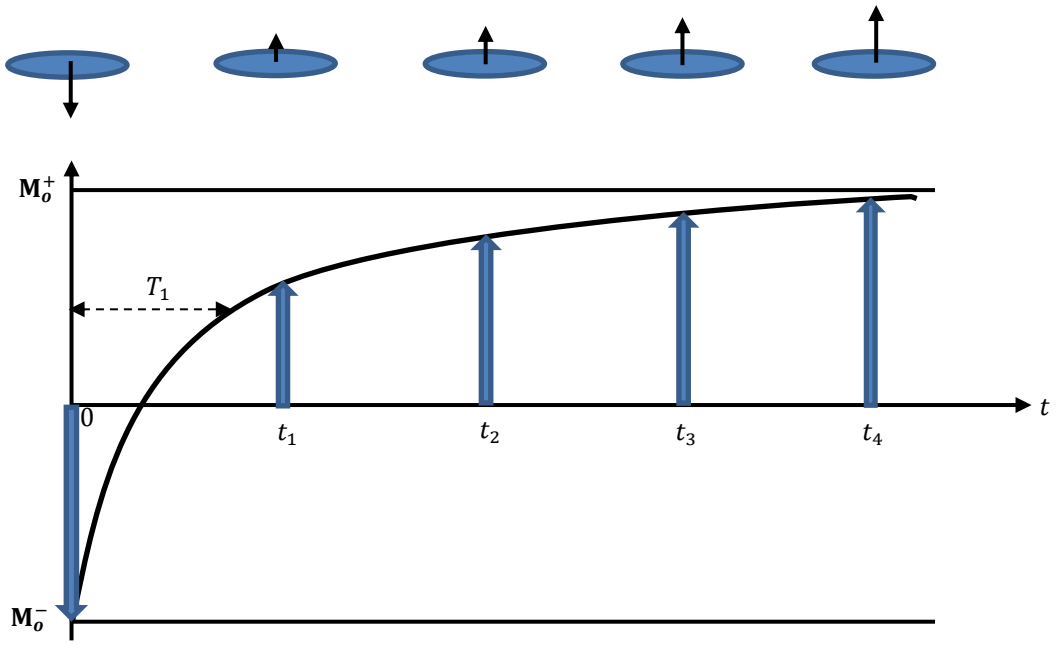

Figure 5.3 Schematic of an inversion recovery process. (Dunn et al. 2002)

5.2 TRANSVERSE RELAXATION

If a current with a frequency equal to the Larmor frequency is applied through a radio frequency (rf) coil placed perpendicular (e.g. the *x* direction), to the direction of a static bar magnet, an oscillatory transverse magnetic field will be generated, with field strength H_1 in the presence of an external static magnetic field H_o. Subsequent application of a 90^0 pulse causes the net magnetization M_o, that was initially precessing in the *z*-direction to tilt into the *xy* plane, in the *y* direction. As soon as this pulse switches off, H_1 becomes zero and the net magnetization M_o, precessing about the *z*-axis gradually moves off the *xy* plane and returns to the *z* direction. This process is known as Free Induction Decay, commonly denoted by T_2*.

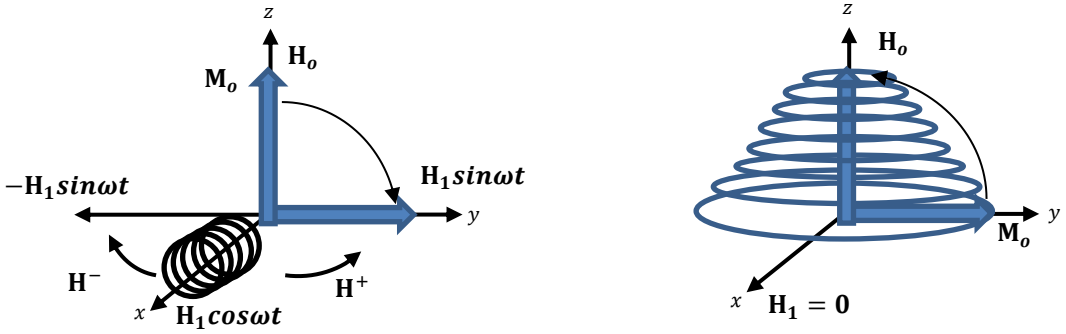

Figure 5.4 Schematic of a Free Induction Decay (FID) pulse. (Dunn et al. 2002)

Two pairs of authors, Carr and Purcell, and Meiboom and Gill came up with a method to remove the complexities associated with measuring T2* as well as other instrument errors. This method involves the use of multiple 180^0 pulse sequences to regenerate several echoes trains of the initial FID signal obtained after the application of an initial 90^0 pulse and it was subsequently named after them as the CPMG spin echo train.

The process is briefly explained as follows. At the onset of the application of an external static magnetic field H_o, the net magnetization vector M_o, builds up to its maximum at thermal equilibrium and points in the positive *z* axis. If another magnetic field H_1, applied in the *x* direction, is imposed on the system by means of electric current (at the Larmor frequency of the protons) applied on a radio frequency coil, the net magnetization will tilt unto the *xy* plane in the *y* direction. If the current to the rf coil is terminated, the pulse from the magnetic field H_1 disappears and as explained previously in the FID concept, the net magnetization vector signal gradually decays from the transverse plane in its return to the longitudinal plane.

However, the net magnetization vector experiences 'dephasing' as it precesses about the z axis on its return to the longitudinal plane. This means that the spins are precessing at different rates. Some at a higher Larmor frequency while others at lower Larmor frequencies. This is owing to the inhomogeneity of the static magnetic field which gives rise to a magnetic field gradient in the z direction. The magnetic field inhomogeneity can be time dependent and also time independent. The time independent components come from heterogeneities within the sample, while the time dependent component arises from the vibration and rotation of neighboring nuclei, (Dunn et al. 2002).

This dephasing causes the dispersion and 'spreading' out of the spins which were originally aligned, as they precess about the z axis along the transverse plane. After a certain period of time τ, a 180^0 pulse is applied to the system in order to 'flip' the spins to the other side of the transverse xy plane. This causes the slower precessing spins which were lagging behind initially, to now lead the faster precessing spins as both spins continue to precess about the z axis. Thus, after another duration of time τ, the spins converge again on the y axis and we observe a resurgence of the initial magnetization signal. This observed signal is called a spin echo.

This process of dephasing, flipping and convergence of spins repeats itself as the spins precess about the z axis and several echoes of the original signal can be obtained by applying multiple 180^0 pulses spaced at a time interval 2τ apart so as to produce an echo train. Each 180^0 pulses reverse the dephasing arising from the previous pulse. The subsequent echoes produced have amplitudes smaller than the original and the time constant T_2, can be calculated from the decay rate of the amplitude of each spin echo in the train, (Dunn et al. 2002).

$$M_y(t) = M_o\left(e^{-\frac{2nt}{T_2}}\right) \qquad (5.3)$$

The schematic below briefly illustrates a typical CPMG pulse sequence for one cycle.

At time $t = 0$

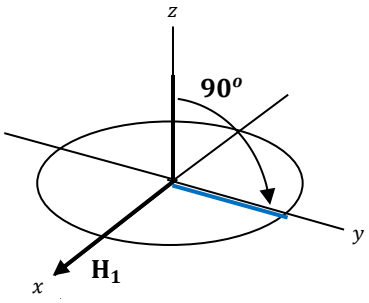

At time $t = 0 < t < \tau$

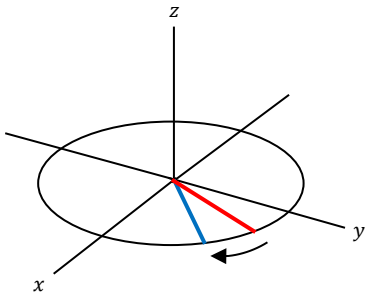

At time $t = \tau$

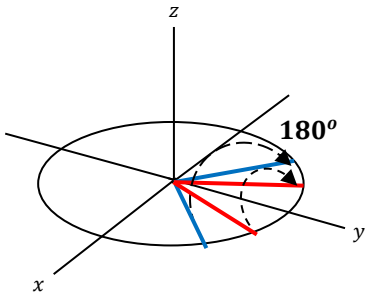

At time $t = \tau < t < 2\tau$

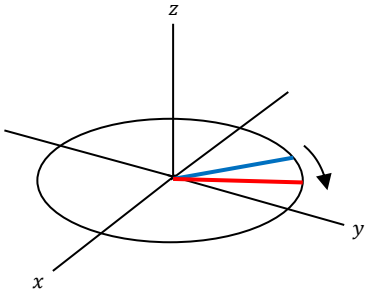

At time $t = 2\tau$

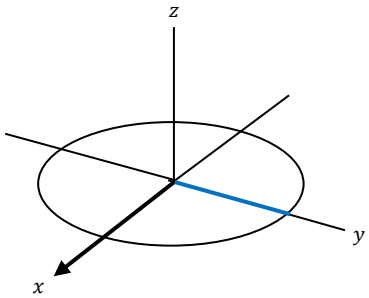

At time $t = 2\tau < t < 3\tau$

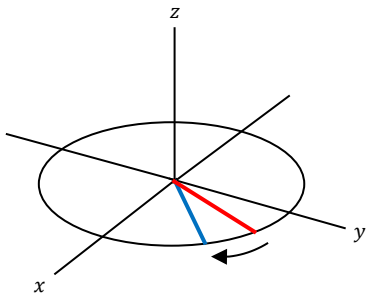

Figure 5.5 Illustration of the CPMG pulse sequence for T_2 measurement. (Chung, 1993)

5.2.1 Diffusion enhanced T2 relaxation

Diffusional effects on T_2 relaxation are insignificant in a perfectly homogeneous magnetic field, because all spin will precess at the same rate regardless of their position within the magnetic field. However, enhanced T_2 measurements can be observed in cases where the molecules of fluids in the pore spaces of rocks are free to move from one region to another, in the presence of magnetic field gradients. In cases where diffusion is significant, this magnetic field gradient arising from the inhomogeneity of the external static magnetic field, causes further dephasing of spins as they precess. The dephasing of spins due to diffusion, only affects T_2 relaxation because it further increases or decreases the rate at which spins precess on the transverse plane, depending on whether they diffuse to regions of higher or lower Larmor frequency. The application of an 180^0 pulse to flip the dephased spins, in a system without nuclei diffusion can refocus the spins but, in a situation, where the effects of diffusion are significant, the spins cannot be refocused because of the continuous random motion of nuclei even after they have been flipped.

However, T_1 measurements on the other hand, are unaffected by diffusion, because longitudinal relaxation is only a measure of the vectoral sum of all magnetic moments pointing in the positive or negative *z* direction. Therefore, regardless of the rate of spin precession about the *z* axis on the *xy* plane, the net magnetic magnetization vector will still point upwards or downwards along the longitudinal axis.

The enhanced T_2 relaxation decay in a magnetic field gradient is given below;

$$M_y(t) = M_o\left(e^{-\frac{2nt}{T_2}-(\gamma\nabla H)^2\frac{2}{3}Dn\tau^3}\right) \qquad (5.4)$$

From the above expression, if the time between echoes τ, is small then the diffusion term is almost negligible. The purpose of the CPMG pulse sequence is to use a small value of τ, to eliminate any possible effect of diffusion on T_2 relaxation in an inhomogeneous static magnetic field.

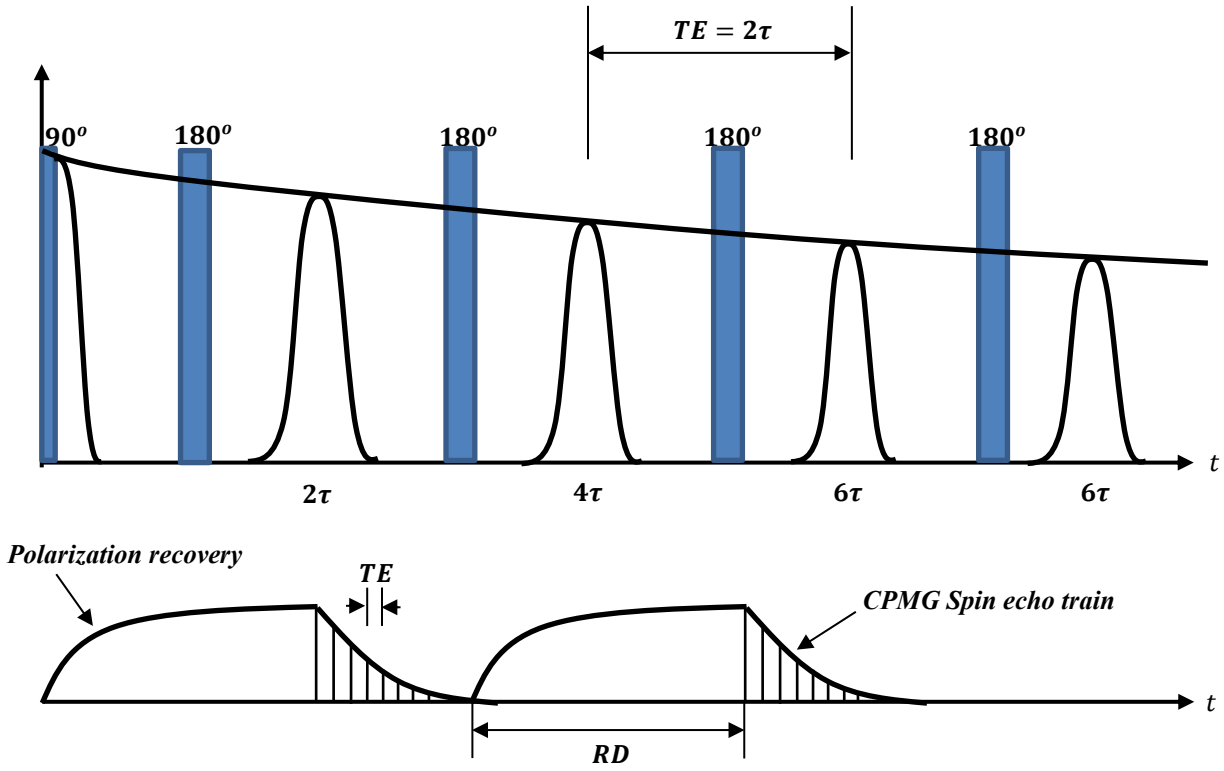

Figure 5.6 Graphical representation of the CPMG spin echo train for T_2 measurements. (Dunn et al. 2002)

5.3 SURFACE RELAXATION

Surface relaxation is a phenomenon observed in rocks that have paramagnetic ions such as iron, manganese etc. existing on the pore walls. It has the capacity to greatly reduce longitudinal and transverse relaxation times and it is of two major mechanisms. The first form occurs on all the non-magnetic sites on the surface, while the second form which is stronger than the first, results from paramagnetic impurities on pore surfaces. The higher the amount of paramagnetic impurities distributed on the pore surface, the higher the surface relaxation, (Dunn et al. 2002).

The surface relaxation affects both T_1 and T_2 and it is related to the pore surface area to volume ratio by the expression below;

$$\frac{1}{T_{1,2}} \approx \frac{\rho S}{V} \tag{5.5}$$

In general, with all factors influencing relaxation considered, the total longitudinal and transverse relaxation rates can be written below as;

$$\frac{1}{T_1} = \frac{1}{T_{1,bulk}} + \frac{1}{T_{1,surface}} \tag{5.6}$$

$$\frac{1}{T_2} = \frac{1}{T_{2,bulk}} + \frac{1}{T_{2,surface}} + \frac{1}{T_{2,diffusion}} \tag{5.7}$$

5.4 Application of NMR Data to EOR in Tight Oil Reservoirs

It is necessary to calibrate NMR magnetization data with known volumes of water so that the signal per unit volume of the saturating fluid, can be obtained. However, before this can be done, it is useful to measure the hydrogen densities of oil or gas with respect to an equal volume of water. This quantity is known as the Hydrogen Index. It is defined as,

$$HI = \frac{Amount\ of\ Hydrogen\ in\ Sample}{Amount\ of\ Hydrogen\ in\ an\ equal\ volume\ of\ Pure\ Water\ at\ standard\ conditions} \tag{5.8}$$

For single component fluids, the expression below given by Dunn et al. (2002), can be used to calculate the HI.

$$HI = \frac{9\rho n_H}{M_W} \tag{5.9}$$

where, ρ is the density of the fluid, n_H is the number of hydrogen atoms in the chemical formula, M_W is the molecular weight and the number 9 in the numerator signifies the ratio of the molecular weight of water, $(18g)$ to the product of the number of hydrogen atoms in water and the density of water $(1g/cm^3)$. The hydrogen index will first be determined before carrying out other NMR measurements.

The Hydrogen Index n-dodecane and water was determined by running a few experiments with known volumes of water and n-dodecane.

PARAMETERS	
Recycle Delay (ms)	18750
Number of Scans	16
Time between echoes (ms)	0.088
T_2 max	2500
Number of Echoes	71023
Points per Echo	1

Table 5.1 Parameters used for both dodecane and water HI measurements

Actual Volume (ml)	NMR Volume (ml)
2	2.0961
4	3.9316
8	7.8196
16	15.3552

Table 5.2 Summary of results for Water.

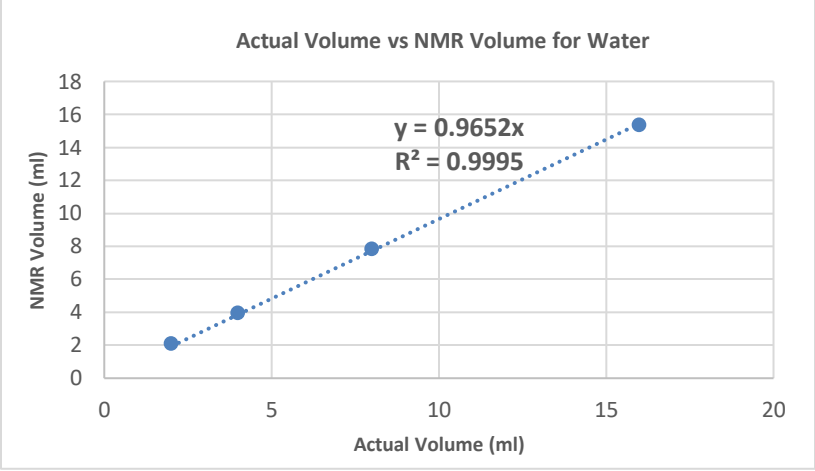

Figure 5.7 HI index measurements for water

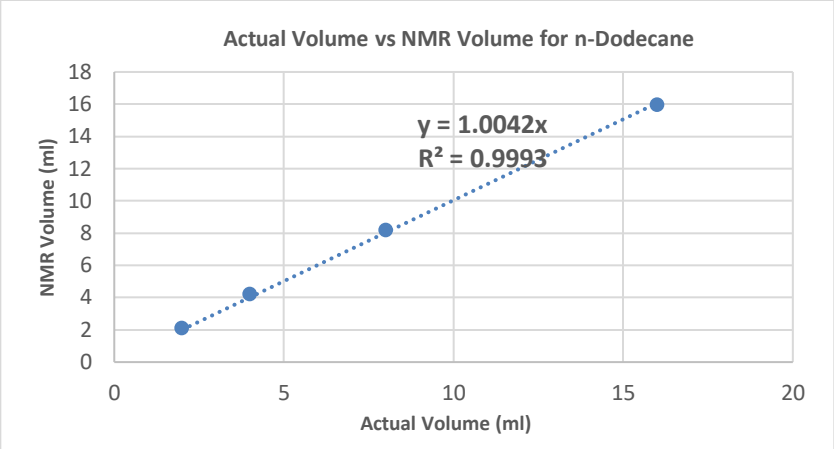

Figure 5.8 HI index measurements for n-Dodecane

Actual Volume (ml)	NMR Volume (ml)
2	2.0850
4	4.2046
8	8.1690
16	15.9428

Table 5.3 Summary of results for n-Dodecane.

5.5 T_2 Distributions and Pore Size Distribution

Data from NMR signals can be used to generate a pore size distribution if only one phase of fluid is present. The magnetization relaxation data within the pores of rocks can be represented by the following expression given by Dunn et al. (2002).

$$M(t) = M_o \sum_{j=1}^{n} \phi_j \, e^{-\frac{t}{T_j}} \qquad (5.10)$$

$$\sum_{j=1}^{n} \phi_j = 1 \qquad (5.11)$$

Where T_j is the surface longitudinal relaxation rate, $M(t)$ is the time dependent relaxation, M_o is the initial magnetization, ϕ_j is the volume fraction of pores with T_j relaxation time and a_j is the pore dimension. The pore size distribution model assumes

that each individual pore is relaxing independently of other pores. For a case where, magnetic data is obtained from a rock that is saturated with a single-phase fluid, the magnetic data can be thought of as a sum of magnetic data originating from the fluids in the different pore sizes each decaying mono-exponentially with a decay rate given by a characteristic time constant T_j. This time constant is proportional to its pore size and an amplitude ϕ_j, also proportional to the volume fraction of its pore sizes (Dunn et al. 2002). To obtain the values of T_j and ϕ_j, (Timur 1968), assumed a two exponential model and tried to minimize the expression below with an appropriate choice of fitting constants; ϕ_a, ϕ_b, T_a, T_b.

$$M(t)/_{M_o} = \phi_a e^{-\frac{t}{T_a}} + \phi_b e^{-\frac{t}{T_b}} \quad (5.12)$$

$$1 = \phi_a + \phi_b \quad (5.13)$$

$$\chi^2 = \sum_{i=1}^{m} \left(\phi_a e^{-\frac{t_i}{T_a}} + \phi_b e^{-\frac{t_i}{T_b}} - M(t_i)/_{M_o} \right)^2 \quad (5.14)$$

The inversion process now involves choosing a set of relaxation time constants T_j, evenly spaced on a logarithmic scale and solving for the amplitudes ϕ_j explicitly. This reduces the minimization expression above from a non-linear to a linear fit problem and provides a framework for assuming a continuous pore size distribution.

5.6 Results from Oil Intrusion Experiments

The pore network and pore structure in organic mudrocks are very complex, because they consist of inter-particle and intra-particle porosity. Inter-particle porosity consists of pore spaces between the grains while intra-particle porosity consists of pores spaces within the grains. The pore size distribution in shale varies from a few micrometers to hundreds of nanometers and as such oil intrusion into these pore spaces require a very high amount of capillary pressure, as opposed to conventional reservoirs

that require lower capillary pressures because they have pore sizes in the range of tens to hundreds of micrometers.

The real magnetization data obtained from each T_2 scan are subtracted from the signal of the dry shale sample. Subtracting the data helps to cancel any background noise, thus, making it possible for the magnetization signal to represent only the effects of oil intrusion into the crushed shale particles. The resulting differential magnetization data is inverted using the least square optimization NMR inversion procedure outlined earlier.

The T_2 distributions shown below, are obtained after inverting the real magnetization signals. The huge peak noticed at small relaxation times is as a result of the fast relaxation coming from the clay and capillary bound water. The other peaks noticed at intermediate relaxation times are indicative of oil intrusion into the intermediate sized pore spaces within the crushed shale sample at various pressures. The differential NMR signals helps to see the effects of oil intrusion into the pore spaces within the shale in greater detail. The cumulative plot - obtained by summing the amplitudes of the T_2 distribution from the differential signal – gives an idea of the amount of oil that has intruded the pore spaces of the crushed sample at a specified pressure. These T_2 distributions give insight on the fluid distribution within the various pore sizes present in the shale. The figure shows oil intrusion into two sets of pore sizes. The small pores with a T_2 cut-off of about 30ms and intermediate pores with a T_2 cut-off of about 300ms.

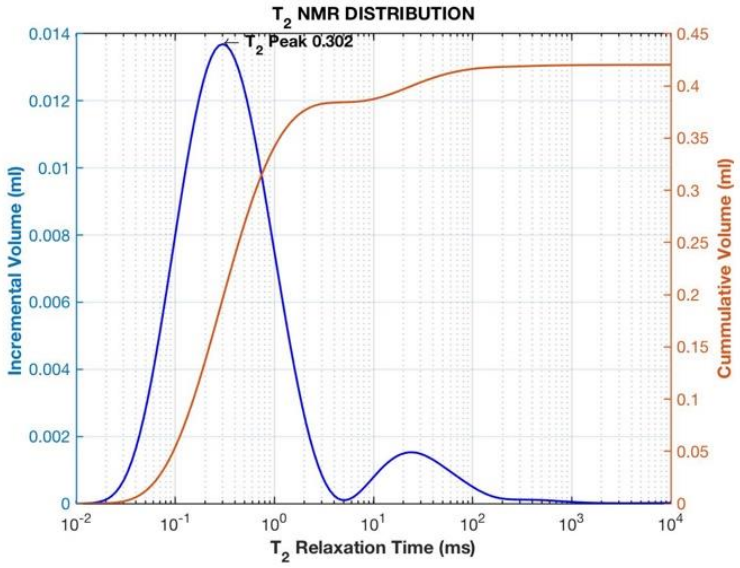

Figure 5.9 T_2 distribution and cumulative T_2 distribution of dry shale

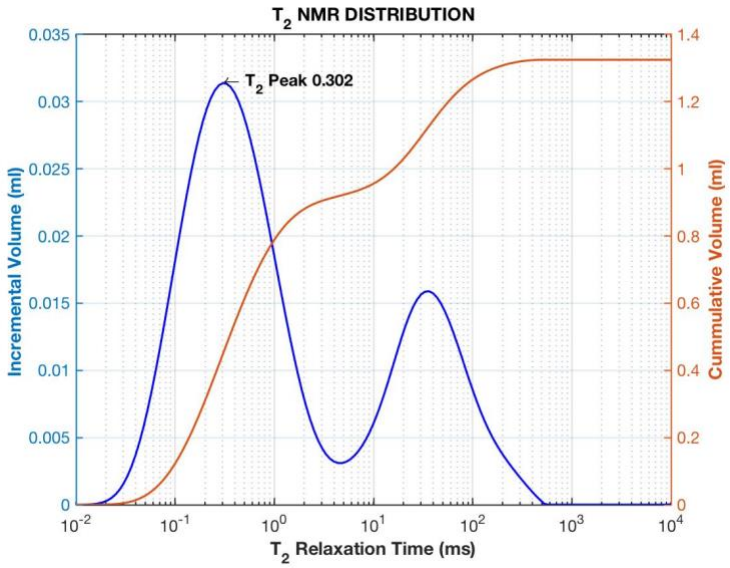

Figure 5.10 T_2 distribution and cumulative T_2 distribution of shale sample at 500 psi

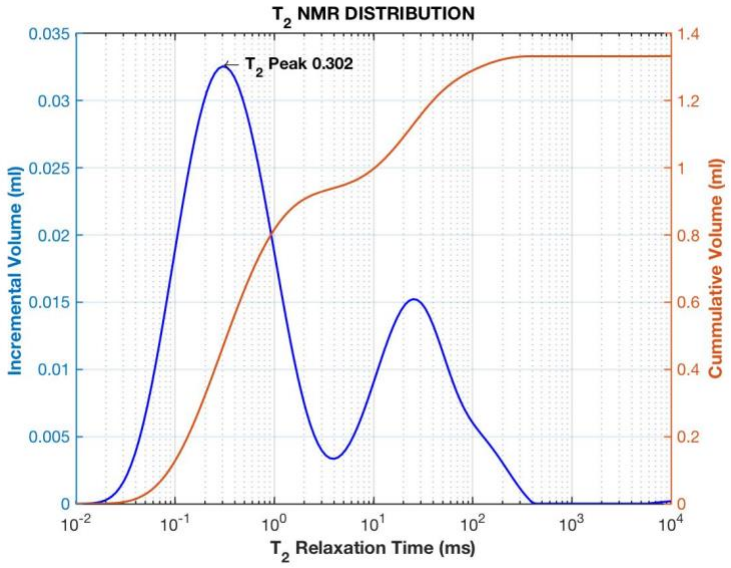

Figure 5.11 T_2 distribution and cumulative T_2 distribution of shale sample at 2000 psi

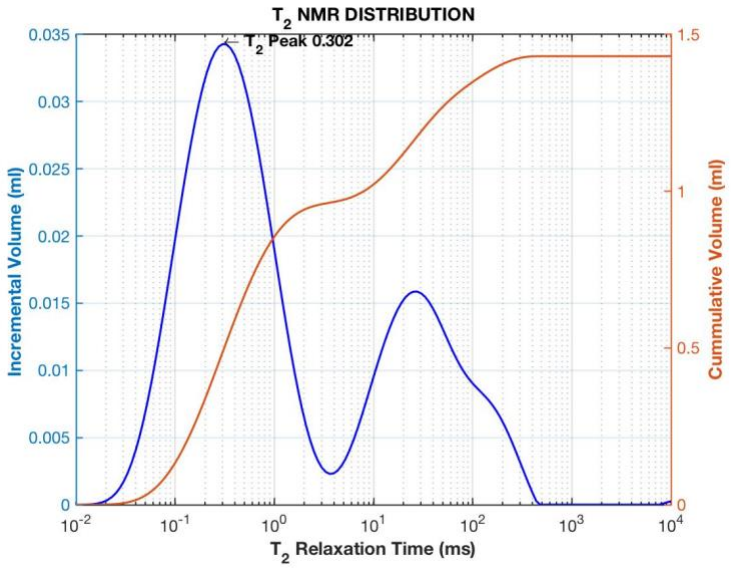

Figure 5.12 T_2 distribution and cumulative T_2 distribution of shale sample at 4000 psi

The observation from the plots above is that at high pressures, dodecane is able to overcome the capillary forces needed to penetrate the small pore sizes. In addition, as evident from the signal coming from the intermediate T_2 relaxation times we see oil

intrusion into the intermediate pore sizes. Super-imposition of T_2 distributions from the differential signals as shown below, at increasing pressure levels show that the peaks line up and are they are increasing in size. This signifies progressive oil intrusion into the small and intermediate pores spaces. The phenomenon shown in the figures below does not show fluid migration. The growth in the peaks at different pressure levels show that oil volume is increasing within these regions. If there was a case of fluid migration, then one peak will be growing at the expense of another, that is the area under the curves will be constant, but one peak will increase in amplitude while the other will decrease. However, we see that both small and intermediate peak amplitudes are increasing as pressure increases.

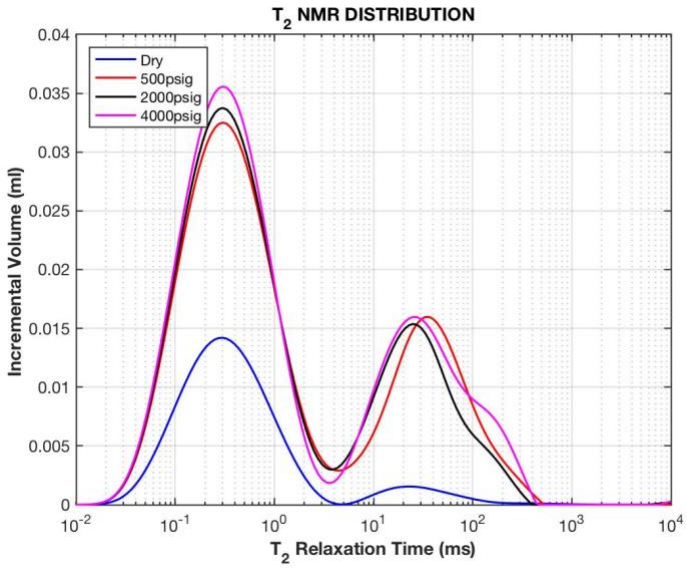

Figure 5.13 T_2 distribution of raw NMR signal before subtraction.

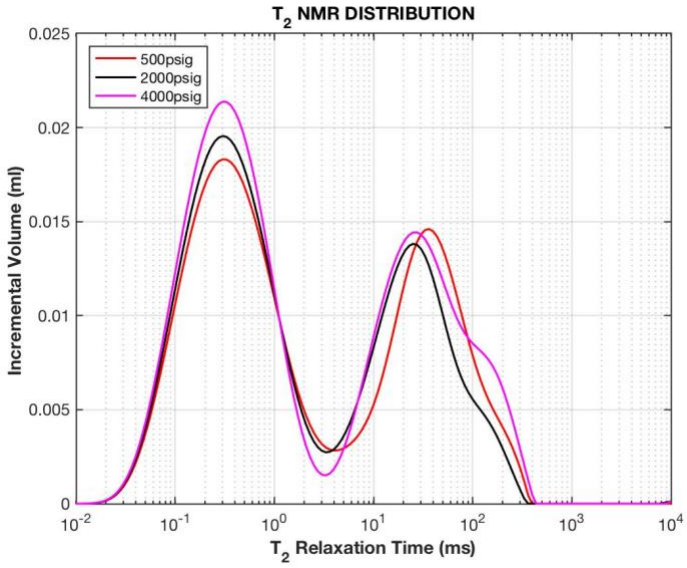

Figure 5.14 Differential T_2 distribution.

5.7 DESCRIPTION OF PARAMETERS USED FOR NMR SPECTROMETRY

5.7.1 Tau

This is the difference in time between the 90° and 180° pulse. A very small value is desirable because it eliminates diffusion effects which greatly influences the T_2 relaxation time. This value was set to 0.052ms.

5.7.2 T_2 max

This is the maximum expected T_2 in the sample. A value of 400ms was used.

5.7.3 Number of Echoes (NE)

This is the number of resurged signals within the spin echo train. It is calculated using τ and T_2 max. The default value was accepted for this parameter.

$$NE = \frac{5 * T_{2max}}{2 * \tau} \qquad (5.15)$$

5.7.4 Number of Points per Echo

This is the number of points that are acquired along each echo. This helps to calculate the signal-noise ratio. A value of 4 was chosen.

5.7.5 Relaxation Delay (RD)

This is the time between successive scans. It is the time observed for the system to return to equilibrium before another scan is performed. If not enough time is left before another scan is performed, then the signal amplitude will be reduced for the next scan because the ultimate magnetization would not have reached it maximum value. The total time for the scan is proportional to RD. The default value was accepted for this parameter.

5.7.6 Number of Scans

This is the number of repeat scans that are used for averaging and calculating the signal – noise ratio. The greater the number of scans, the better the signal to noise ratio (SNR). However, the SNR varies with $\sqrt{NE}$, therefore it is important to choose NSA and SNR wisely.

5.7.7 Receiver Gain

This is the extent of amplification that can be applied to the NMR signal before it is retrieved. If this value is too low, then the resolution of the signal will be small, however, if the gain is too high, then the signal will saturate the receiver.

The table below shows the values that were set for each of these parameters during the experiments.

Parameter	**T_2**	**T_1-T_2**
Recycle Delay (ms)	1500	1000
Number of Scans	–	368
Signal to Noise Ratio	100	–
T_2 max (ms)	200	200
T_1 max (ms)	–	200
Number of Echoes	9434	9434
Number of Steps	–	30
Time between Echoes (ms)	0.053	0.053
Points per Echo	8	8

Table 5.4 Parameters used for the NMR T_2 & T_1-T_2 experiment.

Chapter 6: Summary and Conclusions

This experimental study presented the pressure decline method and its data was used to determine the liquid permeability and capillary pressure drainage curve in a tight rock. The pressure decline versus time data obtained during the procedure, can also be used to estimate fluid saturations as a function of time. This could be very useful in the determination of relative permeability curves in tight rocks.

Furthermore, this work also showed the application of NMR spectroscopy as a useful tool in visualizing fluid distribution within tight rocks. Using a combination of T_1 and T_2 data, progressive oil intrusion could be observed within the inorganic and organic pore spaces.

The choice of crushed shale over shale core plugs for this experimental study was made because crushed particles provide a larger surface area to volume ratio compared to core plugs and this expedited the oil intrusion process. Though, there are concerns that crushing the shale might introduce some artificial porosity which might alter its initial pore structure.

6.1 Conclusions

The results from this experimental study shows that capillary pressure curves in tight rocks can be estimated using the pressure decline method, though this method has not yet been validated, it can be used to estimate liquid permeability and determine fluid saturations as a function of time and pressure. In addition, the pressure decline data showed that oil intrusion was faster within the first few pressure increments, and it gradually slowed as pressure was increased up to 4000 psi.

Also, NMR spectroscopy showed a case of progressive fluid intrusion with an increase in pressure, as opposed to a case of fluid migration or fluid redistribution within the pore spaces. The superimposed T_2 data showed that oil intrusion into small and intermediate sized pores will occur at lower pressures, however, at higher pressures, oil intrusion was only appreciable in the smaller pores. This indicates that at higher pressures, oil is able to overcome the capillary entry pressure for these nano-sized organic pores.

6.2 FUTURE WORK

The tiny pore sizes in tight rocks, suggest high capillary pressures. However, the limitation inherent in the operating conditions of the experimental apparatus used for these initial experiments hindered the application of high pressures. It is intended in the future to perform the same experiments in a pressure vessel that is capable of withstanding internal pressures up to 12,000 psi. This will enable a broader spectrum of the capillary pressure curve to be estimated.

In addition, the principle behind the pressure decline method will be extended in order to generate the imbibition capillary pressure curve so that the effect of capillary pressure hysteresis in tight rocks can be visible. Thereafter, the results from the experiments will be integrated into reservoir simulations to better predict oil production from tight oil reservoirs.

Furthermore, the pressure decline method in conjunction with NMR spectroscopy will be applied to crushed samples of varying particle sizes from several shale outcrops such as the Eagle Ford, Bakken and Utica. A comparison of their respective capillary pressure curves will be carried out in order to see the effects of particle size and pressure increase or decrease on fluid distribution within their pore spaces.

Finally, this novel method will be incorporated into enhanced oil recovery experiments to help estimate the amount and rate of oil recovered during gas injection and solvent injection. This can be accomplished by analyzing the pressure – time data retrieved during the solvent depressurization phase to generate the imbibition curve. The total oil recovery can be computed from the volume difference between the drainage and imbibition curve at a constant pressure.

References

Anderson, W. G., (1986). Wettability Literature Survey, Part 2. Journal of Petroleum Technology, Vol. 38, pp. 1246 – 1262, Nov., 1986.

Altunbay, M., Martian, R., Robinson, M., (2001). Capillary Pressure Data from NMR Logs and its Implications on Field Economics. Presented at the SPE Annual Technical Conference and Exhibition in New Orleans, Louisiana, September 30-October 3, 2001.

Brace, W.F., Walsh, J.B., Frangos, W.T., (1968). Permeability of Granite under High Pressure. Journal of Geophysics Research, 1968.

Brown, H. W., (1951). Capillary Pressure Investigations. Petroleum Transactions, Vol. 192, 1951.

Bruce, W. A., and Welge, H. J., (1947). Restored State Method for Determination of Oil in Place and Connate Water. API Division of Production Amarillo, Texas, May 22-23, 1947.

Charles, P., Egermann, P., Lenormand, J., L. (2007). Low Permeability Measurements using Steady-State and Transient Methods. Institutional Symposium of the society of core analysts September 2007.

Chen, T., Stagg, P.W., (1984). Semilog Analysis of the Pulse-Decay Technique of Permeability Measurement. SPE Journal, December, 1984.

Chen, T., Chen, O., Chen, P., (1998). Capillary Pressure During Immiscible Displacement. Presented at the annual technical meeting of the Petroleum Society in Calgary, June 8 – 10, 1998.

Chung, W. (1993). Inversion of Pulsed NMR Data Using Eigen analysis. M.S. Thesis, Massachusetts institute of technology, Boston, Chicago.

Civian, F., Devegowda, R., Sigal, R., (2013). Improved Data Analysis and Interpretation Method for Laboratory Determination of Crushed-Sample Shale Permeability. Presented at the Canadian Unconventional Resources Conference, Denver, Colorado, August 12 -14, 2013.

Civan, F., Devegowda, D., (2015). Comparison of Shale Permeability to Gas Determined by Pressure-Pulse Transmission Testing of Core Plugs and Crushed Samples.

Presented at the Canadian Unconventional Resources Conference, San-Antonio, Texas, July 20 -22, 2015.

Coates, G.R., Xiao, L., & Prammer, M.G., (1999). NMR Logging Principles and Applications. Halliburton Energy Services, Publication h02308, Ch 2-3, 33-65.

Daigle, H., Johnson, A., Gips, J., Sharma, M. (2014). Porosity Evaluation of Shales Using NMR Secular Relaxation. SPE 1905272. Presented at the Unconventional Resources Technology Conference in Denver, CO. August 25-27, 2014.

Darabi, H., Ettehad, A., Javadpour, F., Sepehrnoori, K., (2012). Gas Flow in Ultra-Tight Strata. Journal of Fluid Mechanics, November, 2012.

DRX Non-Expert User's Manual, (2009). Oxford Instruments Molecular Biotools Ltd., Oxford shire, UK.

DRX Basic Magnetic Resonance Imaging, (2010). Oxford Instruments Molecular Biotools Ltd., Oxford shire, UK.

Dodge, W. Shafer, J. L., Klimentidis, R. E., (1996). Capillary Pressure: The Key to Producible Porosity. Presented at the SPWLA Annual Logging Symposium, June 16 – 19, 1996.

Dunn, K.-J., Bergman, D.J., LaTorraca, G. A., (2002). Nuclear Magnetic Resonance Petrophysical and Logging Applications. Elsevier Science Ltd., UK.

Evans, C. E., and Guerrero, E. T., (1979). Theory and Application of Capillary Pressure. SPWLA twentieth annual logging symposium, June 3 – 6, 1979.

Farissoux, P., Colombian A., Pujol, G., Fraute, O., Nicot, B., (2018). Ultra-Fast Capillary Pressure and Resistivity Measurements. Society of Exploration Geophysicists.

Fleury, M., Samiento, M. R. (2015). Characterization of Shale Using T1-T2 NMR Maps. Journal of Petroleum Technology, (2015), 30172-8.

Forsans, T. M., Schmitt, L., (1994). Capillary Forces: The Neglected Factor in Shale Instability Studies. Presented at the Eurock SPE/ISRM Rock Mechanics in Petroleum Engineering Conference, Delft, Netherlands, August 29 – 31, 1994.

Gao, B., Wu, J., Chen, S., Kwak, H., Funk, J., (2011). New Method for Predicting Capillary Pressure Curves from NMR Data in Carbonate Rocks. Presented at the SPWLA Annual Logging Symposium, Colorado Springs, May 14 - 18, 2011.

Glorioso, J. C., Aguirre, O., Gabriel, P., Mengual, J. F., (2003). Deriving Capillary Pressure and Water Saturation from NMR Transversal Relaxation Times. Presented at the SPE Latin American and Caribbean Petroleum Engineering Conference, Trinidad West-Indies, April 27 – 30, 2003.

Green, D., Dick, J., Veselinovic, D., (2013). Hardware Setup and Calibration Manual. Green Imaging Technologies, Inc. UM8000, R6.0, Ch 4, 73-76.

Green, D., Dick, J., Veselinovic, D., (2013). Hardware Setup and Calibration Manual. Green Imaging Technologies, Inc. UM8021, R6.0, Ch 2, 8-10.

Gips, J., (2014). Shale Characterization Using TGA, Py-GC-MS, and NMR. M.S. Thesis, The University of Texas at Austin.

Jones, S, C., (1997). "A Technique for Faster Pulse-Decay Permeability Measurements in Tight Rocks. March, 1997.

Lake, L. W. 1989. Enhanced Oil Recovery. Upper Saddle River, New Jersey: Prentice Hall.

Lasswell, P., (2013) "Steady-State Permeability analysis in Unconventional Plays. Geo convention, 2013.

Leverett, M. C., (1941). Capillary Behavior in Porous Solids. Trans. AIME, 142, pg. 152 – 169.

Martinez, G. A., Lorne, A. D., (2000). Petrophysical Measurements in Shale Using NMR. Presented at the SPE/AAPG Western Regional Meeting held in Long Beach California, June 19 -23, 2000.

Metwally, Y. M., Sondergeld, C, H., "Measuring low permeabilities of gas-sands and shales using a pressure transmission technique," International Journal of Rock Mechanics and Mining Sciences., (September, 2011).

Newsham, K. E., Rushing, J. A., Lasswell, P. M., Cox, J. C., Blasingame, T. A., (2004). A Comparative Study on Laboratory Techniques for Measuring Capillary Pressure in Tight Gas Sands. Presented at the SPE Annual Technical Conference and Exhibition in Huston, Texas, September 29 -29, 2004.

Nicot, B., Vorapalawut, N., Rousseau, B., Madariaga, L.F., Hamon, G., Korb, J.P., (2016). Estimating Saturation in Organic Shales Using 2D NMR. SCA 2015-024. Presented at the Society of Core Analysts International Symposium, Canada, August 16-21, 2015.

Nojabaei, B., Johns, R. T., (2012). Effect of Capillary Pressure on Fluid Density and Phase Behavior in Tight Rock and Shales. Presented at the SPE Annual Technical Conference and Exhibition in San Antonio, Texas, October, 8 -10, 2012.

Odusina, E., Sondergald, C., Rai, C., (2011). An NMR Study on Shale Wettability. Presented at the Canadian Unconventional Resources Conference, Calgary, November 15 – 17, 2011.

Sander, R., Pan, Z., Connell, L. D., (2016). Laboratory Measurement of Low Permeability Unconventional Gas Reservoir Rocks: A Review of Experimental Methods.

Selvadurai, A.P.S., Carnaffan, P., "A transient pressure pulse method for the measurement of permeability of a cement grout," Canadian journal of civil engineering (1997).

Sondergald, C., Tinni, A., Rai, C., Besov, A., (2016). NMR Considerations in Shale Evaluation. Presented at the SPWLA Annual Logging Symposium, Reykjavik, Iceland, June 25 -29, 2016.

Song, I., Elphick, S.C., Main, I.G., Ngwenya, B.T., Odling, N.W., "One-dimensional fluid diffusion induced by constant-rate flow injection: Theoretical analysis and application to the determination of fluid permeability and specific storage of cored rock samples", Journal of Geophysics Research, (2004).

Sun, B., Yang, E., Wang, H., Seltzer, S.J., Montoya, V., Crowe, J., Malizia, T., (2016). Using NMR to Characterize Fluids in Tight Rock Unconventional and Shale Formations. Presented at the Society of Petrophysicists and Well Log Analysts in Reykjavik, Iceland June 25-29, 2016.

Volokitin, Y., Looyestijin, W., Slijkerman, W., Hoffman, J., (1999). Constructing Capillary Pressure Curves from NMR log data in the presence of Hydrocarbons. Presented at the SPWLA Annual Logging Symposium, May 30 - June 3, 1999.